

Putting the theory into 'burstlet theory': A biophysical model of bursts and burstlets in the respiratory preBötzinger complex

Ryan S. Phillips^{1,‡,*} and Jonathan E. Rubin^{1,*}

*For correspondence:

Ryan.Phillips@seattlechildrens.org
(RSP); jonrubin@pitt.edu (JER)

Present address: [‡]Center for Integrative Biology, Seattle Children's Research Institute, United States of America

Abstract Inspiratory breathing rhythms arise from synchronized neuronal activity in a bilaterally distributed brainstem structure known as the preBötzinger complex (preBötC). In *in vitro* slice preparations containing the preBötC, extracellular potassium must be elevated above physiological levels (to 7–9 mM) to observe regular rhythmic respiratory motor output in the hypoglossal nerve to which the preBötC projects. Reexamination of how extracellular K^+ affects preBötC neuronal activity has revealed that low amplitude oscillations persist at physiological levels. These oscillatory events are sub-threshold from the standpoint of transmission to motor output and are dubbed burstlets. Burstlets arise from synchronized neural activity in a rhythmogenic neuronal subpopulation within the preBötC that in some instances may fail to recruit the larger network events, or bursts, required to generate motor output. The fraction of subthreshold preBötC oscillatory events (burstlet fraction) decreases sigmoidally with increasing extracellular potassium. These observations underlie the burstlet theory of respiratory rhythm generation. Experimental and computational studies have suggested that recruitment of the non-rhythmogenic component of the preBötC population requires intracellular Ca^{2+} dynamics and activation of a calcium-activated non-selective cationic current. In this computational study, we show how intracellular calcium dynamics driven by synaptically triggered Ca^{2+} influx as well as Ca^{2+} release/uptake by the endoplasmic reticulum in conjunction with a calcium-activated non-selective cationic current can explain all of the key observations underlying the burstlet theory of respiratory rhythm generation. Thus, we provide a mechanistic basis to unify the experimental findings on rhythm generation and motor output recruitment in the preBötC.

Introduction

The complex neurological rhythms produced by central pattern generators (CPG) underlie numerous behaviors in healthy and pathological states. These activity patterns also serve as relatively experimentally accessible instances of the broader class of rhythmic processes associated with brain function. As such, CPGs have been extensively studied using a combination of experimental and computational approaches. The inspiratory CPG located in the preBötzinger complex (preBötC) in the mammalian respiratory brainstem is perhaps one of the most intensively investigated CPGs. Despite decades of research, the mechanisms of rhythm and pattern generation within this circuit remain unresolved and highly controversial; however, it appears that the pieces may now be in place to resolve this controversy.

40 Much of the debate in contemporary research into the mechanisms of preBötC rhythm and pattern generation revolves around the roles of specific ion currents, such as I_{NaP} and I_{CAN} (*Koizumi and Smith, 2008; Thoby-Brisson and Ramirez, 2001; Del Negro et al., 2002a; Koizumi and Smith, 2008; Koizumi et al., 2018; Picardo et al., 2019*), and whether the observed rhythm is driven by an emergent network process (*Rekling and Feldman, 1998; Del Negro et al., 2002b, 2005; Rubin et al., 2009; Sun et al., 2019; Ashhad and Feldman, 2020*) and/or by intrinsically rhythmic or pacemaker neurons (*Johnson et al., 1994; Koshiya and Smith, 1999; Peña et al., 2004*). This debate is fueled by seemingly contradictory pharmacological blocking studies (*Del Negro et al., 2002a; Peña et al., 2004; Del Negro et al., 2005; Pace et al., 2007b; Koizumi and Smith, 2008*) and by new experimental studies (*Kam et al., 2013a; Feldman and Kam, 2015; Kallurkar et al., 2020; Sun et al., 2019; Ashhad and Feldman, 2020*) that challenge existing conceptual and computational models about the generation of activity patterns in the preBötC and underlie the so-called *burstlet theory* of respiratory rhythm generation.

53 The conceptual framework of burstlet theory posits that inspiratory oscillations arise from an emergent network process in a preBötC sub-population dedicated to rhythm generation and that a secondary pattern generating sub-population must be recruited in order to generate a full network burst capable of eliciting motor output. This hypothesis is supported by experimental preparations that compared local preBötC neuronal activity and motor output at the hypoglossal (XII) nerve in medullary slices. These studies found that in a low excitability state (controlled by the bath K^+ concentration (K_{bath})), the preBötC generates a regular rhythm featuring a mixture of large and small amplitude network oscillations, dubbed *bursts* and *burstlets*, respectively, with only the bursts eliciting XII motor output (*Kam et al., 2013a*). Moreover, the fraction of low amplitude preBötC events (burstlet fraction) sigmoidally decreases with increasing K_{bath} and only a subset of preBötC neurons are active during burstlets (*Kallurkar et al., 2020*). Importantly, preBötC bursts can be blocked by application of cadmium (Cd^{2+}), a calcium channel blocker, without affecting the ongoing burstlet rhythm (*Kam et al., 2013a; Sun et al., 2019*), supporting the idea that rhythm generation occurs in a distinct preBötC subpopulation from pattern generation and demonstrating that conversion of a burst into a burstlet is a Ca^{2+} -dependent process. Finally, rhythm generation in the burstlet population is hypothesized to result from an emergent network percolation process. This last idea was developed to explain holographic photostimulation experiments, which found that optically stimulating small subsets (4 – 9) of preBötC inspiratory neurons was sufficient to reliably evoke endogenous-like XII inspiratory bursts with delays averaging $255 \pm 45\text{ ms}$ (*Kam et al., 2013b*). The small number of neurons required to evoke a network burst and the extended duration of the delays both differ from what would be predicted by existing computational preBötC models. Additionally, these delays are on a similar timescale to the ramping pre-inspiratory neuronal activity that precedes network-wide inspiratory bursts, leading to the hypothesis that stimulation of this small set of preBötC neurons kicks off an endogenous neuronal percolation process underlying rhythm generation, which could be initiated by the near-coincident spontaneous spiking of a small number of preBötC neurons.

79 The experimental underpinning of burstlet theory challenges current ideas about inspiratory rhythm and pattern generation. However, the proposed mechanisms of burst and burstlet generation remain hypothetical and, to date, there has not been a quantitative model that provides a unified, mechanistic explanation for the key experimental observations or that validates the conceptual basis for this theory. Interestingly, key components of burstlet theory, namely that inspiratory rhythm and pattern are separable processes and that large amplitude network-wide bursts depend on calcium-dependent mechanisms are supported by recent experimental and computational studies. Specifically, *Koizumi et al. (2018); Picardo et al. (2019)* showed that the amplitude (i.e. pattern) of preBötC and XII bursts is controlled, independently from the ongoing rhythm, by the transient receptor potential channel (TRPM4), a calcium-activated non-selective cation current (I_{CAN}). These findings are consistent with burstlet theory, as they demonstrate that rhythm and pattern are separable processes at the level of the preBötC. Moreover, these experimental obser-

vations are robustly reproduced by a recent computational modeling study (**Phillips et al., 2019**), which shows that pattern generation can occur independently of rhythm generation. Consistent with burstlet theory, this model predicts that rhythm generation arises from a small subset of preBötC neurons, which in this model form a persistent sodium (I_{NaP}) dependent rhythrogenic kernel, and that rhythmic synaptic drive from these neurons triggers post-synaptic calcium transients, I_{CaN} activation, and amplification of the inspiratory drive potential, which drives bursting in the rest of the network.

These recent results suggest that conversion of burstlets into bursts may be Ca^{2+} and I_{CaN} dependent, occurring when synaptically triggered calcium transients in non-rhythrogenic preBötC neurons are intermittently large enough for I_{CaN} activation to occur and to yield recruitment of these neurons into the network oscillation. The biophysical mechanism responsible for periodic amplification of Ca^{2+} transients is not known, however. In this computational study, we put together and build upon these previous findings to show that periodic amplification of synaptically triggered I_{CaN} transients by calcium induced calcium release (CICR) from intracellular stores provides a plausible mechanism that can produce the observed conversion of burstlets into bursts and can explain all of the key observations underlying the burstlet theory of respiratory rhythm generation, thus providing a sound mechanistic basis for this conceptual framework.

Results

109 Calcium induced calcium release periodically amplifies intracellular calcium trans- 110 sients

111 Our first aim in this work was to test whether calcium induced calcium release from ER stores could
112 repetitively amplify synaptically triggered Ca^{2+} transients. To address this aim, we constructed a
113 cellular model that includes the endoplasmic reticulum. The model features a Ca^{2+} pump, which
114 extrudes Ca^{2+} from the intracellular space, a sarcoendoplasmic reticulum calcium transport AT-
115 Pase (SERCA) pump, which pumps Ca^{2+} from the intracellular space into the ER, and the Ca^{2+} ac-
116 tivated inositol trisphosphate (IP3) receptor (Fig 1A). To simulate calcium transients synaptically
117 generated from a rhythrogenic source (i.e., burstlets), we imposed a square wave Ca^{2+} current
118 into the intracellular space with varied frequency and amplitude but fixed duration (250 ms) and we
119 monitored the resulting intracellular Ca^{2+} transients. Depending on parameter values used, we
120 observed various combinations of low and high amplitude Ca^{2+} responses, and we characterized
121 how the fraction of Ca^{2+} transients that have low amplitude depends on values selected within the
122 2D parameter space parameterized by Ca^{2+} pulse frequency and amplitude. We found that the
123 fraction of low amplitude Ca^{2+} transients decreases as either or both of the Ca^{2+} pulse frequency
124 and amplitude are increased (Fig. 1B and example traces C1-C4).

125 Bursts and burstlets in a two-neuron preBötC network.

126 Next we tested whether the CICR mechanism (Fig. 1) could drive intermittent recruitment in a re-
127 ciprocally connected two neuron network that includes one intrinsically rhythmic and one non-
128 rhythmic neuron, as a preliminary step towards considering the rhythm and pattern generating
129 sub-populations of the preBötC suggested by burstlet theory (**Kam et al., 2013a; Cui et al., 2016;**
130 **Kallurkar et al., 2020; Ashhad and Feldman, 2020**) and recent computational investigation (**Phillips**
131 **et al., 2019**). In this network, neuron 1 is an I_{NaP} -dependent intrinsically bursting neuron, with a
132 burst frequency that is varied by injecting an applied current, I_{APP} (Fig. 2 A2-A3). The rhythmic
133 bursting from neuron 1 generates periodic postsynaptic currents (I_{Syn}) in neuron 2, carried in part
134 by Ca^{2+} ions, which are analogous to the square wave Ca^{2+} current in Fig 1. The amplitude of the
135 postsynaptic Ca^{2+} transient is determined by the number of spikes per burst (Fig. 2A4) and by the
136 parameter P_{SynCa} , which determines the percentage of I_{Syn} carried by Ca^{2+} ions (see *materials and*
137 *methods* for a full description of these model components). Conversion of a burstlet (isolated neu-
138 ron 1 burst) into a network burst (recruitment of neuron 2) is dependent on CICR (see Fig. 2-Figure

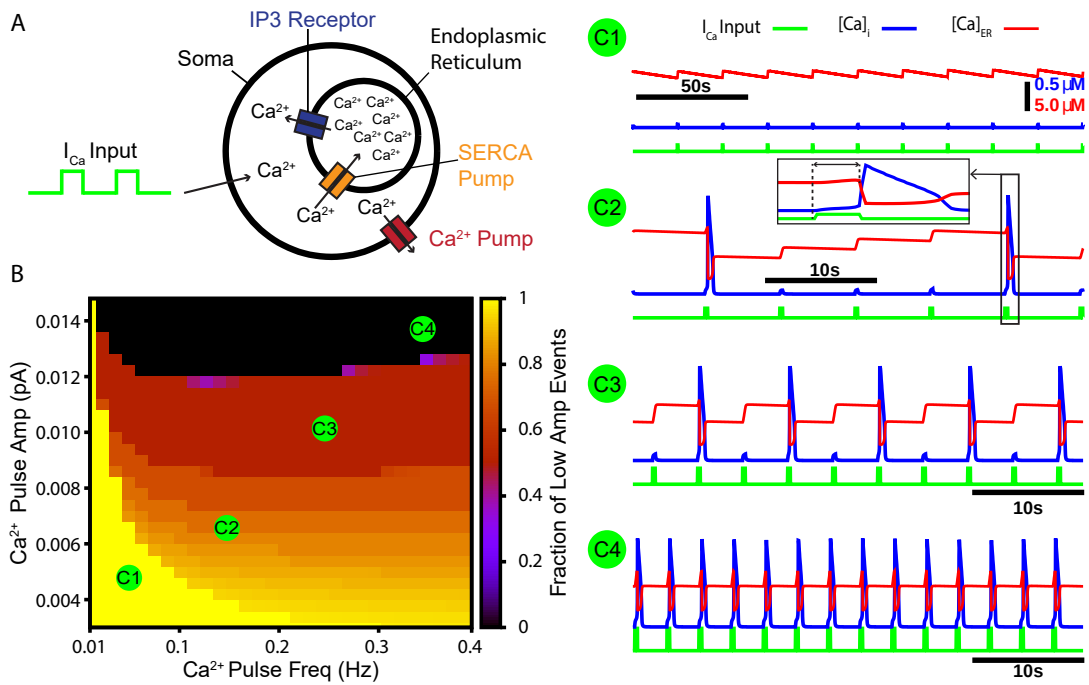


Figure 1. A periodic input in the form of a calcium current drives intermittent calcium induced calcium release from ER stores. (A) Schematic diagram of the model setup showing square wave profile of Ca^{2+} current input into the intracellular space, uptake of Ca^{2+} into the ER by the SERCA pump, Ca^{2+} release through the IP3 receptor, and extrusion of Ca^{2+} through a pump in the cell membrane. (B) Fraction of low amplitude intracellular Ca^{2+} transients as a function of the Ca^{2+} pulse frequency and amplitude. Pulse duration was fixed at 250 ms. (C1-C4) Example traces showing several ratios of low and high amplitude Ca^{2+} transients and the dynamics of the ER stores Ca^{2+} concentration. Inset in C2 highlights the delay between pulse onset and CICR. The pulse amplitude and frequency for each trace are indicated in panel B.

Supplement 1), which increases intracellular calcium above the threshold for I_{CAN} activation.

In the reciprocally connected network, we first quantified the dependence of the burstlet fraction, which was defined as the number of burstlets (neuron 1 bursts without recruitment of neuron 2) divided by the total number of burstlets and network bursts (bursts in neuron 1 with recruitment of neuron 2), on I_{APP} and P_{SynCa} . Increasing I_{APP} increases the burst frequency in neuron 1 and decreases the number of spikes per neuron 1 burst (Fig. 2A3,A4), consistent with past literature (Butera et al., 1999). These changes do not strongly impact the burstlet fraction until I_{APP} grows enough, at which point the shorter, more rapid bursts of neuron 1 become less effective at recruiting neuron 2 and thus the burstlet fraction increases (Fig. 2B2). In general, increasing P_{SynCa} decreased the burstlet fraction (i.e., increased the frequency of neuron 2 recruitment) by causing a larger calcium influx with each neuron 1 burst; see Fig. 2B2 & C1-C4.

The burst frequency in neuron 2 is determined by the burst frequency of neuron 1 and the burstlet fraction. These effects determine the impact of changes in P_{SynCa} and I_{APP} on neuron 2 burst frequency (Fig. 2 B3). As I_{APP} increases, the rise in burstlet frequency implies that neuron 2 bursts in response to a smaller fraction of neuron 1 bursts, yet the rise in neuron 1 burst frequency means that these bursts occur faster. These two effects can balance to yield a relatively constant neuron 2 frequency, although the balance is imperfect and frequency does eventually increase. Increases in P_{SynCa} more straightforwardly lead to increases in neuron 2 burst frequency as the burstlet fraction drops.

Finally, the number of spikes per burst in neuron 2 is not strongly affected by changes in I_{APP} and P_{SynCa} (Fig. 2 B4), suggesting an all-or-none nature of recruitment of bursting in neuron 2. Interestingly, the period between network bursts (i.e., time between neuron 2 recruitment events)

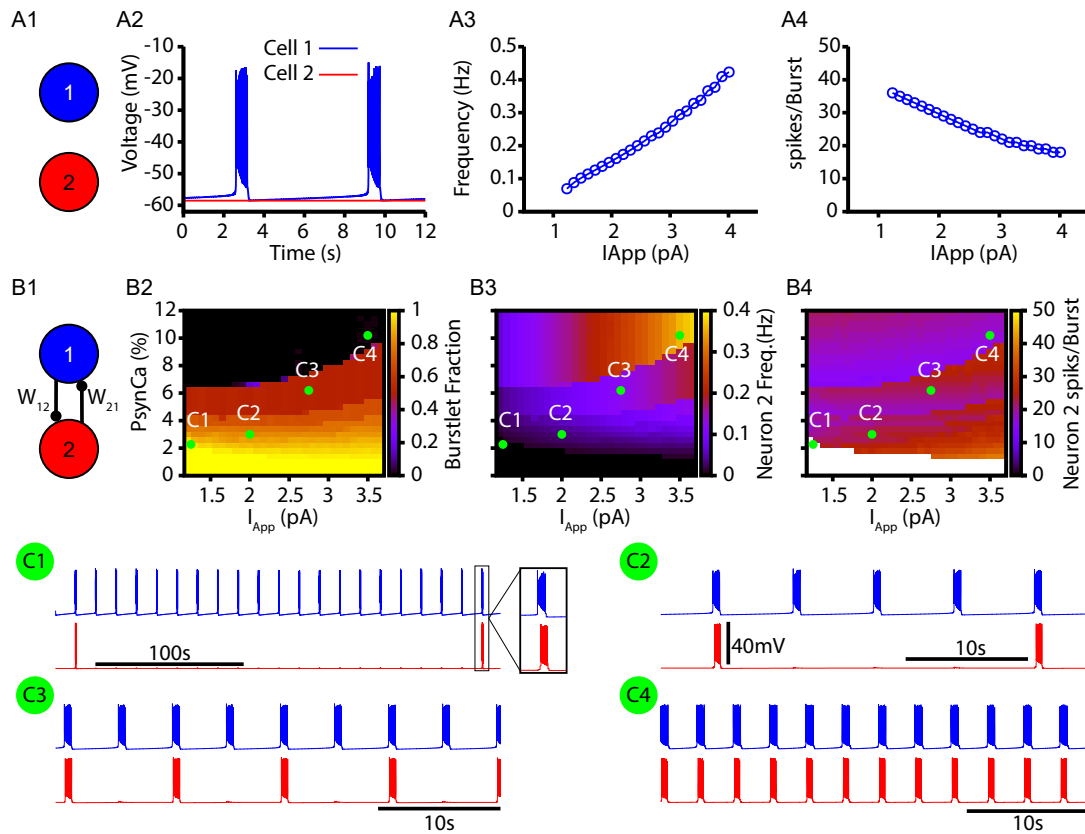


Figure 2. Bursts and burstlets in a two neuron preBötC network. (A1) Schematic diagram of the synaptically uncoupled network. The rhythm and pattern generating components of the network are represented by neuron 1 and 2, respectively. (A2) Example trace showing intrinsic bursting in neuron 1 and quiescence in neuron 2. (A3) Burst frequency and (A4) the number of spikes per burst in neuron 1 as a function of an applied current (I_{APP}). Neuron 2 remained quiescent within this range of I_{APP} . (B1) Schematic diagram of the synaptically coupled network. (B2-B4) 2D plots characterizing the (B2) burstlet fraction, (B3) neuron 2 (burst) frequency, and (B4) neuron 2 spikes per burst (burst amplitude) as a function of I_{APP} and P_{SynCa} . (C1-C4) Example traces for neuron 1 and 2 for various I_{APP} and P_{SynCa} values indicated in (B2-B4). Notice the scale bar is 100 s in C1 and 10 s in C2-C4. Inset in C1 shows the burst shape not visible on the 100 s time scale. The model parameters used in these simulations are: (neuron 1 & 2) $K_{Bath} = 8 \text{ mM}$, $g_{Leak} = 3.35 \text{ nS}$, $W_{12} = W_{21} = 0.006 \text{ nS}$; (Neuron 1) $g_{NaP} = 3.33 \text{ nS}$, $g_{CAN} = 0.0 \text{ nS}$, (Neuron 2) $g_{NaP} = 1.5 \text{ nS}$, $g_{CAN} = 1.5 \text{ nS}$.

161 can be on the order of hundreds of seconds (e.g., Fig. 2 C1). This delay is consistent with some of
 162 the longer timescales shown in experiments characterizing bursts and burstlets (*Kallurkar et al.*,
 163 2020).

164 **CICR supports bustlets and bursts in a data-constrained preBötC network model**

165 Next, we tested whether the CICR mechanism presented in Figs. 1 & 2 could underlie the conversion
 166 of burstlets into bursts in a larger preBötC model network including rhythm and pattern generating
 167 subpopulations and whether this network could capture the K_{bath} -dependent changes in the burst-
 168 let fraction characterized in *Kallurkar et al. (2020)*. K_{bath} sets the extracellular K^+ concentration,
 169 which in turn determines the driving force for any ionic currents that flux K^+ . In preBötC neurons
 170 these currents include the fast K^+ current, which is involved in action potential generation, and the
 171 K^+ -dominated leak conductance, which primarily affects excitability (Fig. 3A). In our simulations,
 172 we modeled the potassium (E_K) and leak (E_{Leak}) reversal potentials as functions of K_{bath} using the
 173 Nernst and Goldman–Hodgkin–Katz equations. The resulting curves were tuned to match existing
 174 data from *Koizumi and Smith (2008)*, as shown in Fig. 3B. In our simulations, we found that intrinsic
 175 bursting is extremely sensitive to changes in K_{bath} . However, with increasing K_{bath} , intrinsic bursting

176 could be maintained over a wide range of K^+ concentrations when accompanied by increases in
 177 g_{Leak} (Fig. 3C). Additionally, the number of spikes per burst in the bursting regime increases with
 178 K_{bath} (Fig. 3 Figure Supplement 1). This K_{bath} -dependence of g_{Leak} is consistent with experimental
 179 data showing that neuronal input resistance decreases with increasing K_{bath} (*Okada et al., 2005*).

180 To construct a model preBötC network, we linked rhythm and pattern generating subpopulations
 181 via excitatory synaptic connections within and between the two populations (Fig. 3D). We dis-
 182 tinguished the two populations by endowing them with distinct distributions of persistent sodium
 183 current conductance (g_{NaP}), as documented experimentally (*Del Negro et al., 2002a; Koizumi and*
 184 *Smith, 2008*). In both populations, we maintained the dependence of g_{Leak} on K_{bath} (see Fig. 3C and
 185 E).

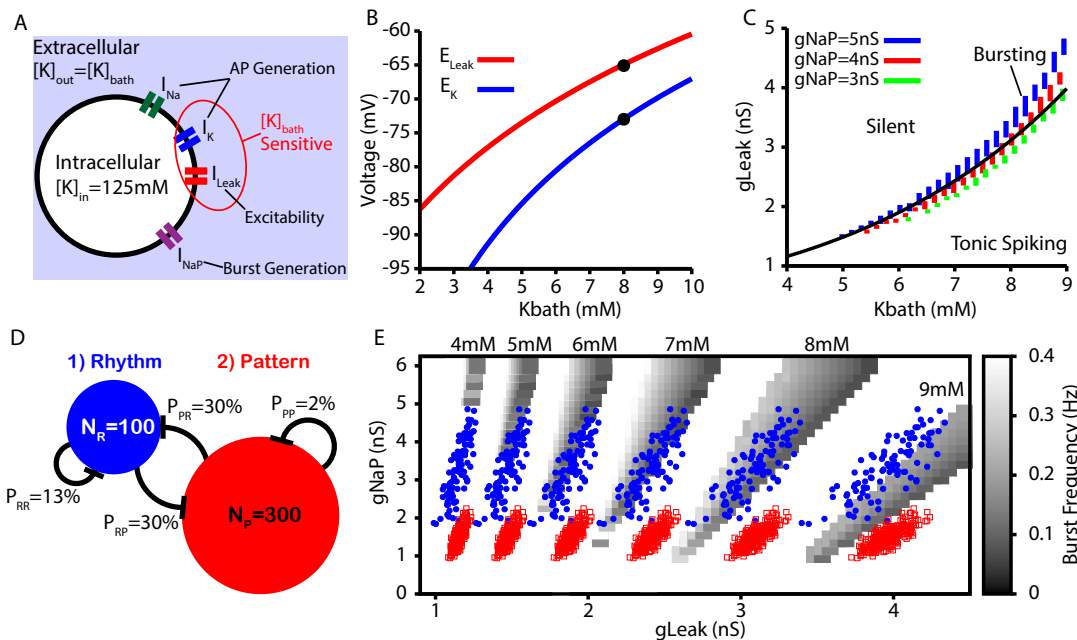


Figure 3. Intrinsic cellular and network dynamics depend on the bath potassium concentration. (A) Schematic diagram of an isolated model preBötC neuron showing the simulated ion channels involved in AP generation, excitability and burst generation as well as indication of currents directly affected by changing the bath potassium concentration (K_{bath}). (B) Dependence of potassium (E_K) and leak (E_{Leak}) reversal potentials on K_{bath} . Black dots indicate experimentally measured values for E_K and E_{Leak} from *Koizumi and Smith (2008)*. (C) Dependence of intrinsic cellular dynamics on K_{bath} , g_{Leak} and g_{NaP} . Black curve represents the relationship between K_{bath} and g_{Leak} used in the full preBötC network. (D) Schematic diagram of size and connectivity probabilities of the rhythm and pattern generating populations within the preBötC model. (E) 2D plot between g_{NaP} and g_{Leak} showing the location of the intrinsic bursting regime for varied concentrations of K_{bath} . The distributions of neuronal conductances in the rhythm and the pattern generating populations are indicated by the blue dots and red squares, respectively.

186 For the full preBötC network model, we first characterized the impact of changes in K_{bath} on net-
 187 work behavior without calcium dynamics by setting $P_{SynCa} = 0$. This network condition is analogous
 188 to *in vitro* preparations where all Ca^{2+} currents are blocked by Cd^{2+} and the preBötC can only gener-
 189 ate burstlets (*Kam et al., 2013a; Sun et al., 2019*). Not surprisingly, with calcium dynamics blocked,
 190 we found that the network can only generate small amplitude network oscillations (burstlets) that
 191 first emerge at approximately $K_{bath} = 5\text{ mM}$ (Fig. 4A). Moreover, under these conditions, increasing
 192 K_{bath} results in an increase in the burstlet frequency and amplitude (Fig. 4B & C), which is consistent
 193 with experimental observations (*Kallurkar et al., 2020*).

194 In the full network with calcium dynamics ($P_{SynCa} > 0$), burstlets generated by the rhythmogenic
 195 subpopulation will trigger postsynaptic calcium transients in the pattern generating subpopulation.
 196 Therefore, in this set of simulations the burstlet activity of the rhythm generating population plays

197 an analogous role to the square wave Ca^{2+} current in Fig. 1 and to bursts of the intrinsically rhythmic
198 neuron in Fig. 2. In this case, the frequency of the postsynaptic Ca^{2+} oscillation is again controlled
199 by K_{bath} and the Ca^{2+} amplitude is determined by the burstlet amplitude and P_{SynCa} . Therefore, for
200 this network, we characterized the burstlet fraction, burst frequency and burst amplitude – with
201 a burst defined as an event in which a burstlet from the rhythm generating population recruits a
202 burst in the pattern generating population – in the full preBötC model network as a function of
203 K_{bath} and P_{SynCa} (Fig. 4E-G). We found that increasing P_{SynCa} or K_{bath} generally decreases the burstlet
204 fraction, increases burst frequency, and slightly increases the burst amplitude (Fig. 4E-G and H1-
205 H4). The decrease in the burstlet fraction with increasing K_{bath} or P_{SynCa} is caused by the increase
206 in the burstlet amplitude (Fig. 4C) or in Ca^{2+} influx with each burstlet, respectively, both of which
207 increase the Ca^{2+} transient in the pattern generating subpopulation. The increase in burst fre-
208 quency with increases in K_{bath} or P_{SynCa} is due to the decreased burstlet fraction (i.e., the burstlet to
209 burst transitions occurs on a greater proportion of cycles) and, in the case of K_{bath} , by an increase
210 in the burstlet frequency (Fig. 4B). The slight increase in burst amplitude with increasing K_{bath} is
211 largely due to the increase in the burstlet amplitude (Fig. 4 C). Fig. 4I highlights the relative shape
212 of burstlets and bursts as well as the delay between burstlet generation and recruitment of the
213 pattern generating population and simulated hypoglossal output. Experimentally, it is likely that
214 postsynaptic Ca^{2+} transients will increase with increasing K_{bath} due to the change in the resting V_m in
215 non-rhythmic preBötC neurons (Tryba et al., 2003) relative to the voltage-gated activation dynam-
216 ics of post-synaptic calcium channels (Elsen and Ramirez, 1998); see Discussion for a full analysis of
217 this point. Interestingly, in our simulations, increasing P_{SynCa} (i.e. the amplitude of the postsynap-
218 tic calcium transients) with K_{bath} (Fig. 4 traces H1-H4) generated K_{bath} -dependent changes in the
219 burstlet fraction that are consistent with experimental observations (Kallurkar et al., 2020); see
220 Fig. 4J.

221 Note that our model includes synaptic connections from pattern generating neurons back to
222 rhythm generating neurons. These connections prolong activity of rhythmic neurons in bursts, rel-
223 ative to burstlets, which in turn yields a longer pause before the next event (e.g., Fig. 4H1). This
224 effect can constrain event frequencies somewhat in the fully coupled network relative to the feed-
225 forward case (e.g., frequencies in Fig. 4B exceed those in Fig. 4F for comparable K_{bath} levels).

226 **Calcium and I_{CAN} block have distinct effects on the burstlet fraction.**

227 Next, we further characterized the calcium dependence of the burstlet to burst transition in our
228 model by simulating calcium blockade or I_{CAN} blockade by a progressive reduction of P_{SynCa} or
229 g_{CAN} , respectively. We found that complete block of synaptically triggered Ca^{2+} transients or I_{CAN}
230 block eliminates bursting without affecting the underlying burstlet rhythm (Fig. 5 A,B). Interestingly,
231 progressive blockades of each of these two mechanisms have distinct effects on the burstlet frac-
232 tion: blocking postsynaptic Ca^{2+} transients increases the burstlet fraction by increasing the num-
233 ber of burstlets required to trigger a network burst, whereas I_{CAN} block only slightly increases the
234 burstlet fraction (Fig. 5C). In both cases, however, progressive blockade smoothly decreases the
235 amplitude of network bursts, (Fig. 5D). The decrease in amplitude in the case of I_{CAN} block is due
236 to derecruitment of neurons from the pattern forming subpopulation and a decrease in the firing
237 rate of the neurons that remain active, whereas in the case of Ca^{2+} block the decrease in amplitude
238 results primarily from derecruitment (Fig. 5E & F). These simulations provide mechanism-specific
239 predictions that can be experimentally tested.

240 **Dose dependent effects of opioids on the burstlet fraction**

241 Recent experimental results by Baertsch et al. (2021) showed that opioid application locally within
242 the preBötC decreases burst frequency but also increases the burstlet fraction. In the preBötC,
243 opioids affect neuronal dynamics by binding to the μ -opioid receptor (μ OR). The exact number of
244 preBötC neurons expressing μ OR is unclear; however, the number appears to be small, with esti-
245 mates ranging from 8 – 50% (Bachmutsky et al., 2020; Baertsch et al., 2021; Kallurkar et al., 2021).

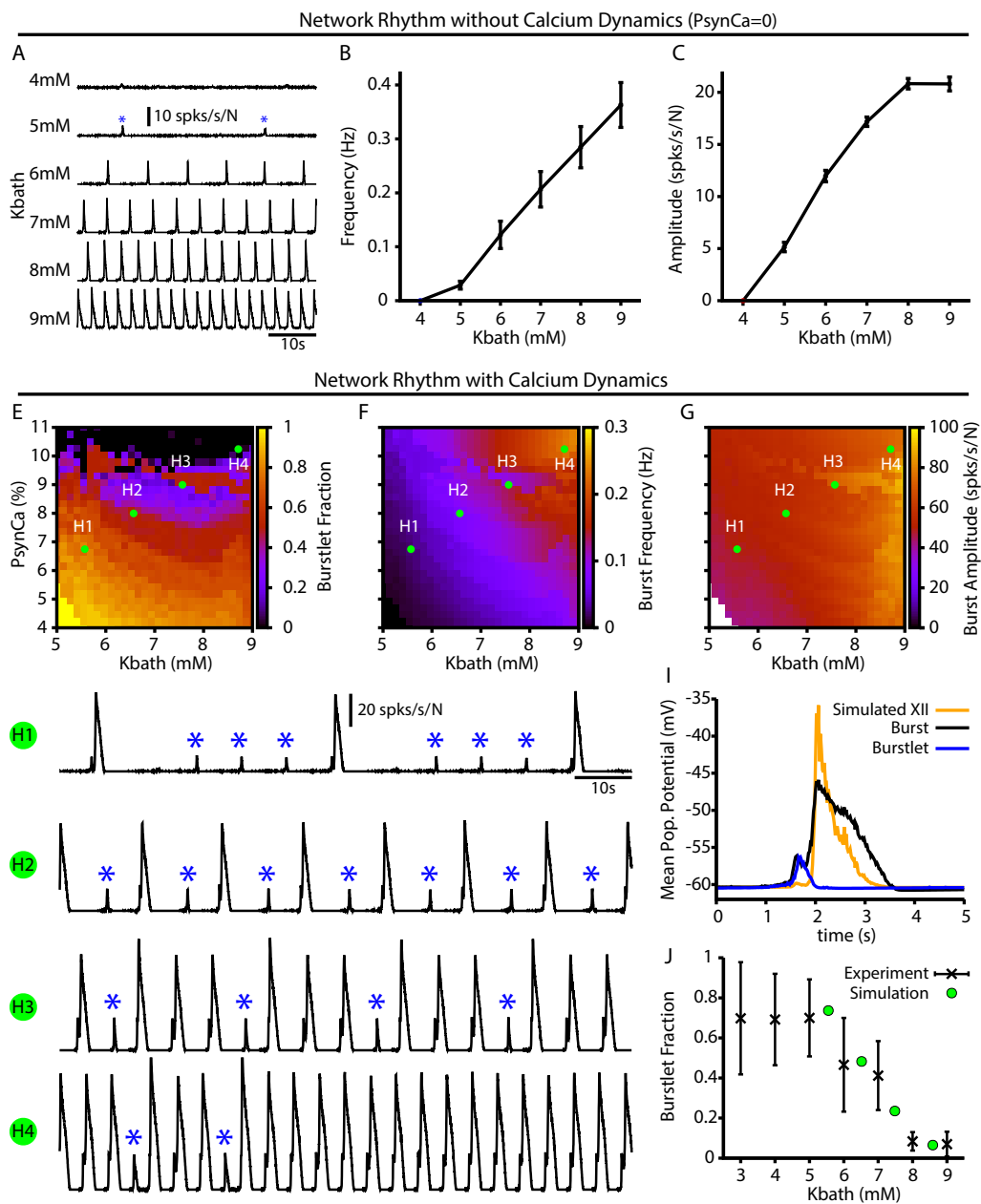


Figure 4. Burstlets and bursts in a 400 neuron preBötC network model with and without calcium dynamics. (A) Rhythmic output of the simulated network without calcium dynamics ($P_{SynCa} = 0$) as a function of K_{bath} . These oscillations are considered burstlets as they are incapable of recruiting the pattern generating population without calcium dynamics. (B) Frequency and (C) amplitude of the burstlet oscillations as a function of K_{bath} . (E-G) 2D plots characterizing the (E) burstlet fraction, (F) the burst frequency, and (G) the burst amplitude as a function of K_{bath} and P_{SynCa} (note that the P_{SynCa} range shown does not start at 0). (H1-H4) Example traces illustrating a range of possible burstlet fractions generated by the network. Burstlets are indicated by asterisks. (I) Overlay of the average population voltage during burst and burstlets. The hypoglossal output is calculated by passing the mean population through a sigmoid function $f = -60.5 + 60/[1 + e^{-(x+45)/2.5}]$. (J) Burstlet fraction as a function of K_{bath} for the four example traces indicated in panels A-C. Experimental data is adapted from [Kallurkar et al. \(2020\)](#).

246 Additionally, μ OR is likely to be selectively expressed on neurons involved in rhythm generation,
 247 given that opioid application in the preBötC primarily impacts burst frequency rather than amplitude ([Sun et al., 2019; Baertsch et al., 2021](#)). Importantly, within the preBötC, opioids ultimately
 248

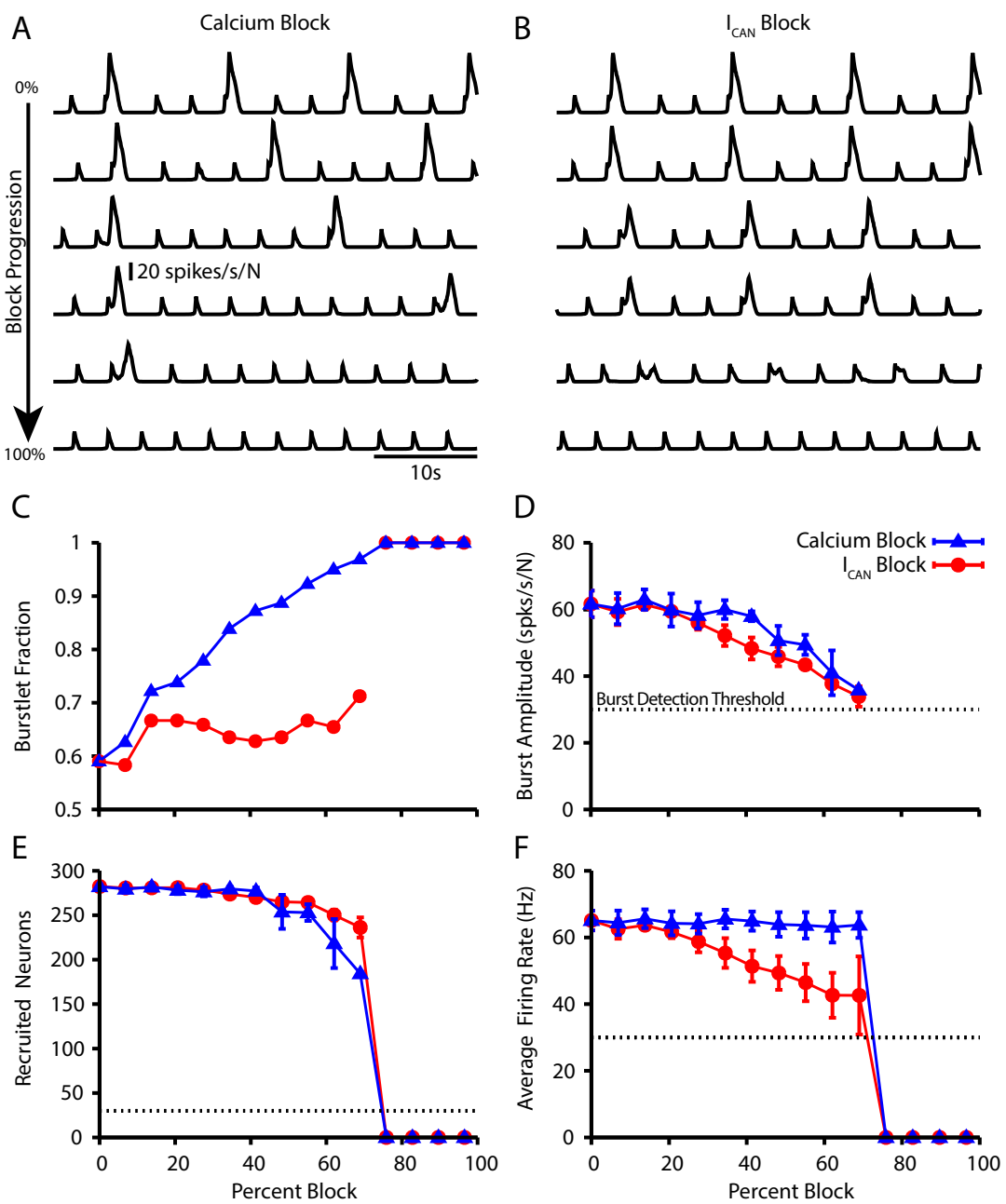


Figure 5. Effect of Ca^{2+} and CAN current blockade on burstlets and bursts. Network traces showing the effect of (A) Calcium current blockade ($P_{\text{Syn}Ca}$ reduction) and (B) CAN current blockade (g_{CAN} reduction) on the period and amplitude of bursts. Effects of calcium or I_{CAN} blockade on (C) the burstlet fraction, (D) the amplitude of bursts and (E) the number of recruited and (F) peak firing rate of recruited neurons in pattern generating subpopulation during network bursts as a function of the blockade percentage.

249 impact network dynamics through two distinct mechanisms: (1) hyperpolarization, presumably
 250 via activation of a G protein-gated inwardly rectifying potassium (GIRK) channel, and (2) decreased
 251 excitatory synaptic transmission, presumably via decreased presynaptic release (Baertsch *et al.*,
 252 2021).

253 Taking these considerations into account, we tested if our model could explain the experimen-
 254 tal observations. Specifically, we simulated opioids as having a direct impact only on the neurons
 255 within the rhythmogenic population and their synaptic outputs (Fig. 6A). To understand how pre-
 256 BötC network dynamics are impacted by the two mechanisms through which opioids have been

257 shown to act, we ran separate simulations featuring either activation of GIRK channels or block
258 of the synaptic output from the rhythmogenic subpopulation (Fig. 6B-F). We found that both GIRK
259 activation and synaptic block reduced the burst frequency (Fig. 6D) and slightly increased burst
260 amplitude (Fig. 6E). The decreased frequency with synaptic block comes from an increase in the
261 burstlet fraction, whereas GIRK activation kept the burstlet fraction constant while reducing the
262 burstlet frequency (Fig. 6F). Finally, combining these effects, we observed that simultaneously in-
263 creasing the GIRK channel conductance and blocking the synaptic output of μ OR-expressing neu-
264 rons in our simulations generates slowing of the burst frequency and an increase in the burstlet
265 fraction consistent with *in vitro* experimental data (Fig. 6D-G).

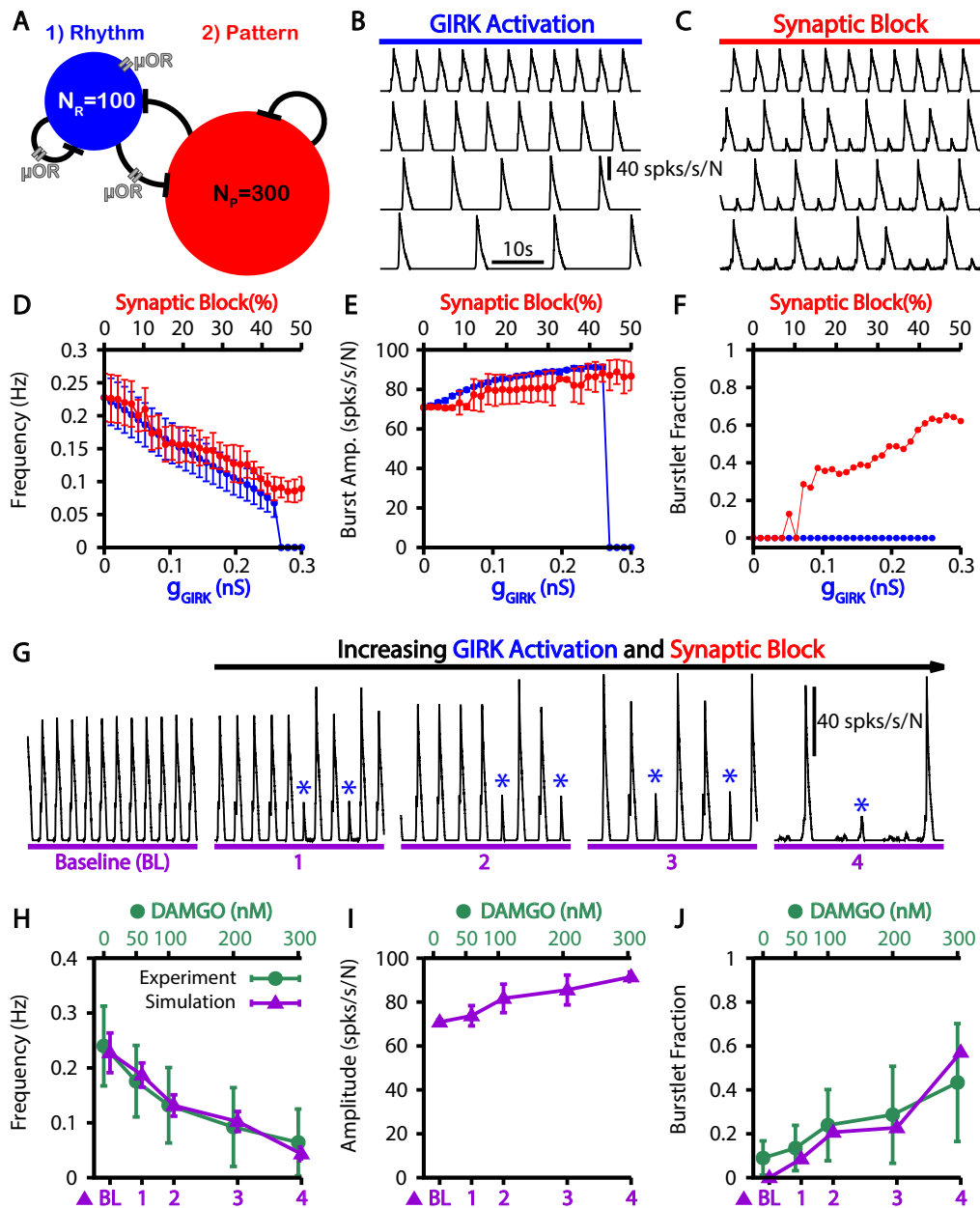


Figure 6. Simulated μ -opioid receptor (μOR) activation by local DAMGO application in the preBötC and comparison with experimental data. (A) Schematic preBötC network diagram showing the location of μOR . Example traces showing the effect of (B) g_{GIRK} channel activation and (C) synaptic block on the network output. Quantification of g_{GIRK} activation or synaptic block by μOR on the (D) burst frequency, (E) burst amplitude and (F) burstlet fraction. Error bars indicate SD. (G) Example traces showing the affects of progressive increases in g_{GIRK} and synaptic block on network output. Burstlets are indicated by blue asterisks. The parameters for each case are as follows: (BL) $g_{\text{GIRK}} = 0.0 \text{ nS}$, $\gamma_{\mu\text{OR}} = 0.0$; (1) $g_{\text{GIRK}} = 0.031034 \text{ nS}$, $\gamma_{\mu\text{OR}} = 0.81034$; (2) $g_{\text{GIRK}} = 0.093103 \text{ nS}$, $\gamma_{\mu\text{OR}} = 0.7069$; (3) $g_{\text{GIRK}} = 0.14483 \text{ nS}$, $\gamma_{\mu\text{OR}} = 0.68966$; (4) $g_{\text{GIRK}} = 0.19655 \text{ nS}$, $\gamma_{\mu\text{OR}} = 0.58621$. Comparison of experimental data and the affects of progressive increases in g_{GIRK} and synaptic block on the (H) frequency and (I) amplitude of bursts as well as (J) the burstlet fractions for the traces shown in (G). Experimental data (H, J) was adapted from Baertsch et al. (2021); however, the changes in amplitude (I) were not quantified.

266 **Simultaneous stimulation of subsets of preBötC neurons elicits network bursts**
 267 **with long delays**
 268 Simultaneous stimulation of 4-9 preBötC neurons in *in vitro* slice preparations has been shown to
 269 be sufficient to elicit network bursts with similar patterns to those generated endogenously (Kam

270 *et al., 2013b*). These elicited bursts occur with delays of several hundred milliseconds relative to
271 the stimulation time, which is longer than would be expected from existing models. Interestingly,
272 in the current model, due to the dynamics of CICR, there is a natural delay between the onset of
273 burstlets and the recruitment of the follower population that underlies the transition to a burst.
274 Therefore, we investigated if our model could match and explain the observations seen in *Kam*
275 *et al. (2013b)*.

276 In our model, we first calibrated our stimulation to induce a pattern of spiking that is comparable
277 to the patterns generated in (*Kam et al., 2013b*) (10-15 spikes with decrementing frequency,
278 Fig. 7A). We found that stimulation of 3-9 randomly selected neurons could elicit network bursts
279 with delays on the order of hundreds of milliseconds (Fig. 7B & C). Next we characterized (1) the
280 probability of eliciting a burst, (2) the delay in the onset of elicited bursts, and (3) the variability in
281 delay, each as a function of the time of stimulation relative to the end of an endogenous burst
282 (i.e., a burst that occurs without stimulation) and of the number of neurons stimulated (Fig. 7D-F).
283 In general we found that increasing the number of stimulated neurons increases the probability
284 of eliciting a burst and decreases the delay between stimulation and burst onset. Moreover, the
285 probability of eliciting a burst increases and the delay decreases as the time after an endogenous
286 burst increases (Fig. 7G,H). Additionally, with its baseline parameter tuning, our model had a refrac-
287 tory period of approximately 1 s following an endogenous burst during which stimulation could not
288 evoke a burst (Fig. 7). The refractory period in our model is longer than measured experimentally
289 (500 ms) (*Kam et al., 2013b*).

290 To conclude our investigation, we examined how changes in the connection probability within
291 the pattern forming population (P_{PP}) affect the refractory period, probability, and delay of evoked
292 bursts following simultaneous stimulation of 3-9 randomly selected neurons in the preBötC popula-
293 tion. We focused on the pattern forming population because it comprises 75% of the preBötC popu-
294 lation and, therefore, neurons from this population are most likely to be stimulated and the synap-
295 tic projections from these neurons are most likely to impact the properties of evoked bursts. These
296 simulations were conducted with fixed network synaptic strength, defined as $S = N_p \cdot P_{PP} \cdot W_{PP}$,
297 where W_{PP} is adjusted to compensate for changes in P_{PP} to keep S constant.

298 With this scaling, we found that decreasing/increasing P_{PP} decreased/increased the refractory
299 period (Fig. 8A-C) by impacting the probability of eliciting a burst in the period immediately after
300 an endogenous burst (Fig. 8D-E). More specifically, the change in the probability of evoking a burst,
301 with decreased/increased P_{PP} , is indicated by a leftward/rightward shift in the probability vs stim-
302 ulation time curves relative to a control level of P_{PP} ($P_{PP} = 2\%$); see Fig. 8D,E. That is, relatively small
303 connection probabilities with large connection strengths lead to network dynamics with a shorter
304 refractory period when stimulation cannot elicit a burst and a higher probability that a stimulation
305 at a fixed time since the last burst will evoke a new burst.

306 It may seem surprising that networks with smaller connection probabilities exhibit a faster
307 emergence of bursting despite their larger connection weights, since intuitively, with lower connec-
308 tion probabilities, fewer neurons could be recruited by each action potential, resulting in longer,
309 more time-consuming activation pathways. A key point, however, is that when connection weights
310 are larger, fewer temporally overlapping inputs are needed to recruit each inactive neuron. For ex-
311 ample, fix N_p and W_{PP} , take P_{PP} to scale as $1/N_p$, and assume that with this W_{PP} , at least r inputs
312 from active neurons are needed to activate an inactive neuron. We can approximate the expected
313 number of neurons receiving r or more inputs from A active neurons by the expected number
314 receiving r inputs, given by

$$\binom{A}{r} \left(\frac{1}{N_p}\right)^r \left(1 - \frac{1}{N_p}\right)^{A-r}.$$

315 If we double P_{PP} , halve W_{PP} , and assume that now at least $2r$ inputs are needed for activation, then

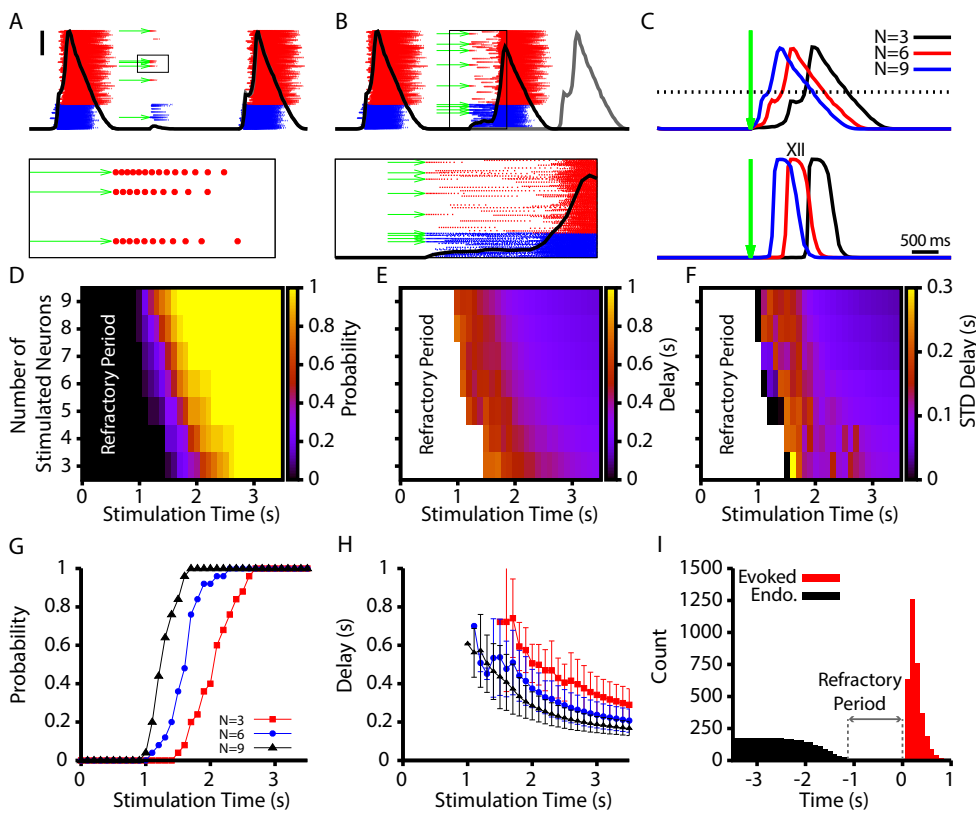


Figure 7. Evoked population bursts by simulated holographic stimulation of 3-9 preBötC neurons. (A) Raster plot of neuronal spiking triggered by simulated holographic stimulation of 6 preBötC neurons shortly after an endogenous burst and resulting failure to evoke a network burst. Black line represents the integrated population activity. Scale bar indicates 20 spikes/s/N. (Bottom panel) shows the spiking activity triggered in individual neurons by the simulated holographic stimulation. Panel duration is 1 s. (B) Example simulation where stimulation of 9 preBötC neurons evokes a network burst. Gray curve indicates timing of the next network burst if the network was not stimulated. (Bottom panel) Expanded view of the percolation process that is triggered by holographic stimulation on a successful trial. Panel duration is 1.75 s. (C) Example traces showing the delay between the stimulation time and the evoked bursts as a function of the number of neurons stimulated for the (top) integrated preBötC spiking and (bottom) simulated hypoglossal activity. (D-F) Characterization of (D) the probability of evoking a burst, (E) the mean delay of evoked bursts, and (F) the standard deviation of the delay as a function of the time after an endogenous burst and the number of neurons stimulated. (G) Probability and (H) delay as a function of the stimulation time for stimulation of 3, 6 or 9 neurons. Error bars in (H) indicate SD. (I) Histogram of evoked and endogenous bursts relative to the time of stimulation ($t = 0$ s) for all successful trials in all simulations; notice a 1 s refractory period.

316 the corresponding approximation becomes

$$\binom{A}{2r} \left(\frac{2}{N_p} \right)^{2r} \left(1 - \frac{2}{N_p} \right)^{A-2r}.$$

317 This is a smaller quantity than the first one for relevant parameter values (such as $N_p = 300$ and
 318 small r as indicated by the stimulation experiments), showing that increasing P_{PP} and proportion-
 319 ally scaling down W_{PP} reduces the chance of successful recruitment of inactive neurons by active
 320 neurons.

321 Interestingly, our simulations suggest that the connection probability in the pattern generating
 322 population must be between 1% and 2% to match the approximately 500 ms refractory period mea-
 323 sured experimentally (Kam et al., 2013b) (Fig. 8F). Surprisingly, the mean and distribution of delays
 324 from stimulation to burst for all successfully elicited bursts are not strongly affected by changes
 325 in P_{PP} (Fig. 8F). For a given stimulation time and number of neurons stimulated, however, decreas-
 326 ing P_{PP} decreases the delay of elicited bursts (Fig. 8G). Finally, because the neurons in the pattern

327 generating population appear to play a dominant role in determining if stimulation will elicit a net-
328 work burst, we characterized how the number of pattern generating neurons stimulated, out of
329 a total set of 9 stimulated neurons, affects the probability of eliciting a network burst as a func-
330 tion of stimulation time (Fig. 8H). These simulations were carried out under a baseline condition of
331 $P_{PP} = 2\%$. In general, we found that stimulating a relatively larger proportion of pattern generating
332 neurons increased the probability of eliciting a network burst for all times after the approximately
333 1 s refractory period, as indicated by the positive slope in Fig. 8H.

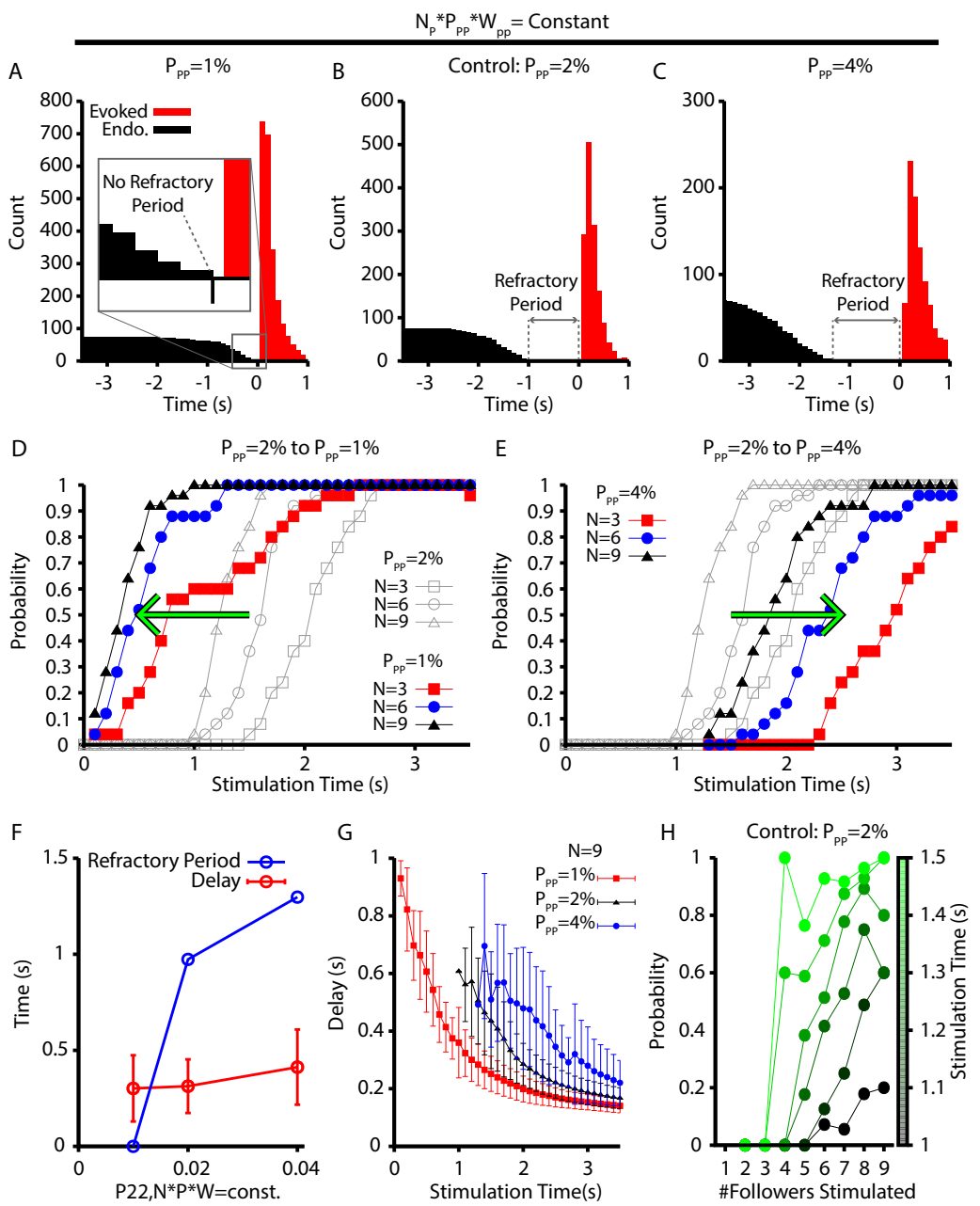


Figure 8. Refractory period and delay of evoked bursts following simulated holographic stimulation depends on the follower network connectivity. (A-C) Histogram of evoked and endogenous bursts relative to the time of stimulation ($t = 0$ s) for all successful trials where 3, 6 and 9 neurons were stimulated and for different connection probabilities (but fixed total network synaptic strength; i.e., $N_p \cdot P_{pp} \cdot W_{pp} = \text{constant}$) in the follower population: (A) $P_{pp} = 1\%$; (B) $P_{pp} = 2\%$; and (C) $P_{pp} = 4\%$. (D & E) Effect of (D) decreasing ($2\% \rightarrow 1\%$) and (E) increasing ($2\% \rightarrow 4\%$) the connection probability in the follower population, P_{pp} . (F) Refractory period and delay from stimulation to burst as functions of the connection probability for the simulations shown in A-E, with $N \cdot P \cdot W = \text{const}$. Error bars indicate SD. Notice that the refractory period increases with increasing connection probability. (G) Effect of P_{pp} on the delay to evoked bursts. (H) Probability of evoking a burst as a function of time (colorbar) and the number out of 9 stimulated neurons that are follower neurons for the baseline case of 2% connection probability.

334 Discussion

335 Recent experiments have revealed a decoupling of respiratory rhythm generation and output pat-
336 ttering in the preBötC, which has given rise to the conceptual framework of burstlet theory. To
337 date, however, this theory lacks the quantitative basis, grounded in underlying biophysical mech-
338 anisms, needed for its objective evaluation. To address this critical gap, in this computational study
339 we developed a data-constrained biophysical model of the preBötC that generates burstlets and
340 bursts as proposed by burstlet theory, with a range of features that match experimental observa-
341 tions. To summarize, we first show that calcium induced calcium release (CICR) from intracellular
342 stores is a natural mechanism to periodically amplify postsynaptic calcium transients needed for
343 I_{CAN} activation and recruitment of pattern-forming neurons into network bursts (Fig. 1). Next,
344 we demonstrate that in a two-neuron network, CICR can convert baseline rhythmic activity into
345 a mixture of bursts and burstlets, where the burstlet fraction depends largely on the magnitude
346 of postsynaptic calcium transients (Fig. 2). In a larger preBötC network containing rhythm- and
347 pattern-forming subpopulations with experimentally constrained intrinsic properties, population
348 sizes and synaptic connectivity probabilities (Fig. 3), similar but more realistic activity patterns arise
349 (Fig. 4). Moreover, we show that this model can match all of the key experimental underpinnings of
350 burstlet theory, including the dependence of the burstlet fraction on extracellular potassium con-
351 centration (Fig. 4 I), the Ca^{2+} dependence of the burstlet-to-burst transition (Fig. 5), the effects of
352 opioids on burst frequency and burstlet fraction (Fig. 6), and the long delay and refractory period
353 of bursts evoked by holographic photostimulation of small subsets of preBötC neurons (Fig. 7 & 8).

354 Insights into the mechanisms of burst (pattern) and burstlet (rhythm) generation 355 in the inspiratory preBötC

356 Burstlet theory to date has largely been an empirical description of the observed features of bursts
357 and burstlets. One idea that has been suggested is that rhythm generation is driven by a stochastic
358 percolation process in which tonic spiking across the rhythm-generating population gradually syn-
359 chronizes during the inter-burst-interval to generate the burstlet rhythm. Subsequently, a burst
360 (i.e. motor output) only occurs if the burstlet is of sufficient magnitude, resulting from sufficient
361 synchrony, to trigger all-or-none recruitment of the pattern-forming subpopulation (*Kam et al., 2013a,b; Feldman and Kam, 2015; Cui et al., 2016; Kallurkar et al., 2020; Ashhad and Feldman, 2020*

362>). This theory, however, does not identify or propose specific biophysical mechanisms capa-
363 ble of generating a quantitative explanation of the underlying cellular and network level dynam-
364 ics, fails to capture the Ca^{2+} dependence of the burst-to-burstlet transition, and cannot explain
365 how extracellular potassium concentration impacts the burstlet fraction. Our simulations support
366 an alternative view that builds directly from previous computational studies (*Jasinski et al., 2013; Phillips et al., 2019; Phillips and Rubin, 2019; Phillips et al., 2021*), which robustly reproduce a
367 wide array of experimental observations. Specifically, in this study we show that amplification of
368 postsynaptic calcium transients in the pattern-generating subpopulation (triggered by burstlets)
369 provides a natural mechanism capable of explaining the Ca^{2+} dependence of the burstlet-to-burst
370 transition.

371 Importantly, we find that the burstlet fraction is determined by the probability that a burstlet
372 will trigger CICR in the pattern forming subpopulation. In the model, this probability is determined
373 by the magnitude of postsynaptic calcium transients as well as the activation dynamics of the IP3
374 receptor and the SERCA pump. Therefore, to explain the decrease in the burstlet fraction with
375 increasing extracellular K_{bath} , the magnitude of the burstlet-triggered postsynaptic calcium trans-
376 tients must increase with K_{bath} . Some of this rise can result directly from the increase in burstlet
377 amplitude with increasing K_{bath} (see (*Kallurkar et al., 2020*) and Fig. 4 C). To fully match the exper-
378 imentally observed relationship between K_{bath} and the burstlet fraction (Fig. 4 J), we also explicitly
379 increased the parameter P_{SynCa} , which sets the proportion of the postsynaptic calcium current car-
380 ried by Ca^{2+} . Thus, our model predicts that the magnitude of postsynaptic Ca^{2+} transients triggered
381

383 by EPSPs should increase as K_{bath} is elevated.

384 This same prediction arises from considering the voltage-dependent properties of Ca^{2+} chan-
385 nels characterized in preBötC neurons and the changes in the membrane potential of non-rhythrogenic
386 (i.e. pattern-forming) neurons as a function of K_{bath} . Specifically, it is likely that voltage-gated
387 calcium channels are involved in generating the postsynaptic Ca^{2+} transients, as dendritic Ca^{2+}
388 transients have been shown to precede inspiratory bursts and to be sensitive to Cd^{2+} , a calcium
389 channel blocker (*Del Negro et al., 2011*). Consistent with this idea, Cd^{2+} -sensitive Ca^{2+} channels in
390 preBötC neurons appear to be primarily localized in distal dendritic compartments (*Phillips et al.,*
391 *2018*). Voltage-gated calcium channels in the preBötC start to activate at approximately -65 mV
392 (*Elsen and Ramirez, 1998*) and importantly, the mean somatic resting membrane potential of non-
393 rhythrogenic preBötC neurons increases from -67.034 mV to -61.78 mV when extracellular potas-
394 sium concentration is elevated from 3 mM to 8 mM (*Tryba et al., 2003*). Moreover, at $K_{Bath} = 9\text{ mM}$,
395 EPSPs in the preBötC are on the order of $2 - 5\text{ mV}$ (*Kottick and Del Negro, 2015; Morgado-Valle*
396 *et al., 2015; Baertsch et al., 2021*) and the amplitude of EPSCs has been shown to decrease as K_{bath}
397 is lowered (*Okada et al., 2005*). Putting together these data on resting membrane potential and
398 EPSP sizes, we deduce that when $K_{Bath} = 3\text{ mM}$, the magnitude of EPSPs may not reach voltages
399 sufficient for significant activation of voltage-gated Ca^{2+} channels. As K_{bath} is increased, however,
400 increases in the membrane potential of pattern-forming neurons and EPSP magnitude are pre-
401 dicted to increase the magnitude of EPSPs triggered by postsynaptic calcium transients. This is
402 exactly the effect that is captured in the model by an increase in P_{SynCa} .

403 The idea that dendritic post-synaptic Ca^{2+} transients and I_{CAN} activation play a critical role in
404 regulating the pattern of preBötC dynamics is well supported by experimental and computational
405 studies. Specifically, the dendritic Ca^{2+} transients that precede inspiratory bursts (*Del Negro et al.,*
406 *2011*) have been shown to travel in a wave to the soma, where they activate TRPM4 currents (I_{CAN})
407 (*Mironov, 2008*). Moreover, the rhythmic depolarization of otherwise non-rhythrogenic neurons
408 (inspiratory drive potential) depends on I_{CAN} (*Pace et al., 2007a*), while the inspiratory drive poten-
409 tial is not dependent on Ca^{2+} transients driven by voltage-gated calcium channels expressed in the
410 soma (*Morgado-Valle et al., 2008*). Finally, pharmacological blockade of TRPM4 channels, thought
411 to represent the molecular correlates of I_{CAN} , reduces the amplitude of preBötC motor output
412 without impacting the rhythm. These experimental findings were incorporated into and robustly
413 reproduced in a recent computational model (*Phillips et al., 2019*). Consistent with these findings,
414 this previous model suggests that rhythm generation arises from a small subset of preBötC neu-
415 rons, which form an I_{NaP} -dependent rhythrogenic kernel (i.e. burstlet rhythm generator), and
416 that rhythmic synaptic drive from these neurons triggers post-synaptic calcium transients, I_{CAN}
417 activation, and amplification of the inspiratory drive potential, which spurs bursting in the rest of
418 the network. The current study builds on this previous model by explicitly defining rhythm- and
419 pattern-generating neuronal subpopulations (see Fig. 3) and by incorporating the mechanisms re-
420 quired for CICR and intermittent amplification of post-synaptic calcium transients.

421 Calcium-induced calcium release mediated by the SERCA pump and the IP3 receptor has long
422 been suspected to be involved in the dynamics of preBötC rhythm and/or pattern generation (*Pace*
423 *et al., 2007a; Crowder et al., 2007; Mironov, 2008; Toporikova et al., 2015*) and has been explored
424 in individual neurons and network models of the preBötC (*Toporikova and Butera, 2011; Jasinski*
425 *et al., 2013; Rubin et al., 2009; Wang and Rubin, 2020*). Experimental studies have not clearly es-
426 tablished the role of CICR from ER stores in respiratory circuits, however. For example, *Mironov*
427 (*2008*) showed that the transmission of calcium waves that travel from the dendrites to the soma is
428 blocked by local application of thapsigargin, a SERCA pump inhibitor. In a separate study, however,
429 block of the SERCA pump by bath application of thapsigargin ($2 - 20\text{ }\mu\text{M}$) or cyclopiazonic acid (CPA)
430 ($30 - 50\text{ }\mu\text{M}$) did not significantly affect the amplitude or frequency of hypoglossal motor output in
431 *in vitro* slice preparations containing the preBötC. It is possible that the negative results presented
432 by the latter work occur due to the failure of pharmacological agents to fully penetrate the slice
433 and diffuse across the cell membranes to reach their intracellular targets. Alternatively, the role of

434 CICR may be dynamically regulated depending on the state of the preBötC network. For example
435 the calcium concentration at which the IP₃ receptor is activated is dynamically regulated by IP₃
436 (*Kaftan et al., 1997*) and therefore, activity- or neuromodulatory-dependent changes in the cyto-
437 plasmic Ca^{2+} and/or IP₃ concentration may impact ER Ca^{2+} uptake and release dynamics. Store
438 operated Ca^{2+} dynamics are also impacted by the transient receptor potential canonical 3 (TRPC3)
439 channels (*Salido et al., 2009*), which are expressed in the preBötC, and manipulation of TRPC3 has
440 been shown to impacted burst amplitude and regularity (*Tryba et al., 2003; Koizumi et al., 2018*)
441 as would be predicted by this model. It is also possible that calcium release is mediated by the
442 ryanodine receptor, an additional calcium activated channel located in the ER membrane (*Lanner*
443 *et al., 2010*), since bath application of CPA (100 μM) and ryanodine (10 μM) removed large ampli-
444 tude oscillations in recordings of preBötC population activity (*Toporikova et al., 2015*).

445 Finally, we note that while various markers can be used to define distinct subpopulations of neu-
446 rons within the preBötC, our model cannot determine which of these ensembles are responsible
447 for rhythm and pattern generation. Past experiments have examined the impact of optogenetic
448 inhibition, applied at various intensities to subpopulations associated with specific markers, on the
449 frequency of inspiratory neural activity, but this activity was measured by motor output, not within
450 the preBötC itself (*Tan et al., 2008; Cui et al., 2016; Koizumi et al., 2016*). According to burstlet the-
451 ory and our model, slowed output rhythmicity could derive from inhibition of rhythm-generating
452 neurons, due to a reduced frequency of burstlets, and from inhibition of pattern-generating neu-
453 rons, due to a reduced success rate of burst recruitment. Thus, measurements within the preBötC
454 will be needed in order to assess the mapping between subpopulations of preBötC neurons and
455 roles in burstlet and burst production.

456 Additional comparisons to experimental results

457 In our model, a burstlet rhythm first emerges at a K_{bath} of approximately 5 mM, whereas in the ex-
458 periments of *Kallurkar et al. (2020)*, the burstlet rhythm continues even down to 3 mM. To explain
459 this discrepancy, we note that our model assumes that the extracellular potassium concentration
460 throughout the network is equal to K_{bath} . Respiratory circuits appear to have some buffering ca-
461 pacity, however, such that for K_{bath} concentrations below approximately 5 mM the extracellular K^+
462 concentration remains elevated above K_{bath} (*Okada et al., 2005*). The K_{bath} range over which our
463 model generates a rhythm would extend to that seen experimentally if extracellular K^+ buffering
464 were accounted for. This buffering effect can also explain why the burstlet fraction remains con-
465 stant in experimental studies when K_{bath} is lowered from 5 mM to 3 mM (*Kallurkar et al., 2020*). Our
466 model also does not incorporate short-term extracellular potassium dynamics that may impact the
467 ramping shape of burstlet onset (*Abdulla et al., 2021*).

468 Although our model incorporates various key biological features, it does not include some of
469 the biophysical mechanisms that are known to shape preBötC patterned output or that are hypothe-
470 sized to contribute to the properties described by burstlet theory. For example, the M-current
471 associated with KCNQ potassium channels has been shown to impact burst duration by contribut-
472 ing to burst termination (*Revill et al., 2021*). Additionally, intrinsic conductances associated with
473 a hyperpolarization-activated mixed cation current (I_h) and a transient potassium current (I_A) are
474 hypothesized to be selectively expressed in the pattern- and rhythm-generating preBötC subpopu-
475 lations (*Picardo et al., 2013; Phillips et al., 2018*). Thus, our model predicts that while these currents
476 may impact quantitative properties of burstlets and bursts, they are not critical for the presence of
477 burstlets and their transformation into bursts. Finally, the current model does not include a popu-
478 lation of inhibitory preBötC neurons. Inhibition is involved in regulating burst amplitude (*Baertsch*
479 *et al., 2018*), but it does not have a clear role in burst or burstlet generation, and therefore inhibi-
480 tion was omitted from this work.

481 Importantly, our model does robustly reproduce all of the key experimental observations un-
482 derlying burstlet theory. Not surprisingly, block of calcium transients or I_{CAN} in our model elimi-
483 nates bursts without affecting the underlying rhythm (Fig. 5), which is consistent with experimental

484 observations (*Kam et al., 2013b; Sun et al., 2019*). Interestingly, our model also provides the exper-
485 imentally testable predictions that blocking calcium transients will increase the burstlet fraction
486 while I_{CAN} block will have no effect on this fraction, whereas both perturbations will smoothly re-
487 duce burst amplitude. Interestingly, the calcium-dependent mechanisms that we include in our
488 model pattern-generating population have some common features with a previous model that
489 suggested the possible existence of two distinct preBötC neuronal populations responsible for
490 eupneic burst and sigh generation, respectively, which also included excitatory synaptic transmis-
491 sion from the former to the latter (*Toporikova et al., 2015*). In the eupnea-sigh model, however,
492 the population responsible for low-frequency, high-amplitude sighs was capable of rhythmic burst
493 generation even without synaptic drive, in contrast the pattern-generation population as tuned in
494 our model. Also in contrast to the results on bursts considered in our study, sigh frequency in the
495 earlier model did not vary with extracellular potassium concentration and sigh generation required
496 a hyperpolarization-activated inward current, I_h .

497 We also considered the effects of opioids in the context of burstlets and bursts, a topic that
498 has not been extensively studied. It is well established that opioids slow the preBötC rhythm in
499 *in vitro* slice preparations; however, the limited results presented to date on effects of opioids on
500 the burstlet fraction are inconsistent. Specifically, *Sun et al. (2019)* found that application of the μ -
501 opioid receptor agonist DAMGO at 10 nM and 30 nM progressively decreased the preBötC network
502 frequency but had no impact on the burstlet fraction before the network rhythm was eventually
503 abolished at approximately 100 nM. Similarly, *Baertsch et al. (2021)* found that DAMGO decreased
504 the preBötC network frequency in a dose-dependent fashion; however, in these experiments the
505 network was less sensitive to DAMGO, maintaining rhythmicity up to approximately 300 nM, and
506 the burstlet fraction increased with increasing DAMGO concentration. The inconsistent effects
507 of DAMGO on the burstlet fraction across these two studies can be explained by our simulations
508 based on the different sensitivities of these two preparations to DAMGO and the two distinct mech-
509 anisms of action of DAMGO on neurons that express μ OR – decreases in excitability and decreases
510 in synaptic output of neurons – identified by *Baertsch et al. (2021)*. In our simulations we show
511 that the decreased excitability resulting from activation of a GIRK channel only impacts frequency,
512 whereas decreasing the synaptic output of μ OR-expressing neurons results in an increase in the
513 burstlet fraction and a decrease in burst frequency (Fig. 6). In experiments, suppression of synap-
514 tic output does not appear to occur until DAMGO concentrations are above approximately 50 nM
515 (*Baertsch et al., 2021*). Therefore, it is not surprising that DAMGO application did not strongly
516 impact the burstlet fraction before the rhythm was ultimately abolished in *Sun et al. (2019)*, due
517 to the higher DAMGO sensitivity of that particular experimental preparation, as indicated by the
518 lower dose needed for rhythm cessation.

519 Mixed-mode oscillations

520 Mixed-mode oscillations, in which intrinsic dynamics of a nonlinear system naturally lead to alterna-
521 tions between small- and large-amplitude oscillations (*Del Negro et al., 2002c; Bertram and Rubin,*
522 *2017*), are a mechanism that has been previously proposed to underlie bursts and burstlets, under
523 the assumption of differences in intrinsic oscillation frequencies across preBötC neurons (*Bacak*
524 *et al., 2016*). This mechanism was not needed to explain the generation of bursts and burstlets
525 in the current model, however. Moreover, systems with mixed-mode oscillations can show a wide
526 range of oscillation amplitudes under small changes in conditions and only emerge when K_{bath} el-
527 evated above 9 mM (*Del Negro et al., 2002c*). These properties are not consistent with the burst
528 and burstlet amplitudes or K_{bath} -dependent changes in the burstlet fraction seen experimentally
529 (*Kallurkar et al., 2020*) and in our model.

530 Holographic photostimulation, percolation and rhythm generation

531 Experimental data supporting burstlet theory has shown that burstlets are the rhythmogenic event
532 in the preBötC. However, although burstlet theory is sometimes referenced as a theory of respi-

533 ratory rhythm generation, the actual mechanisms of burstlet rhythm generation remain unclear.
534 One idea that has been suggested is that rhythm generation is driven by a stochastic percola-
535 tion process in which tonic spiking across the rhythm-generating population gradually synchro-
536 nizes during the inter-burst-interval to generate the burstlet rhythm (**Ashhad and Feldman, 2020**;
537 **Slepukhin et al., 2020**). In this framework, a burst (i.e. motor output) only occurs if the burstlet is
538 of sufficient magnitude, resulting from sufficient synchrony, to trigger all-or-none recruitment of
539 the pattern-forming subpopulation (**Kam et al., 2013a,b; Feldman and Kam, 2015; Kallurkar et al.,**
540 **2020; Ashhad and Feldman, 2020; Slepukhin et al., 2020**).

541 The idea that burstlets are the rhythmogenic event within the preBötC is supported by the ob-
542 servation that block of voltage-gated Ca^{2+} channels by Cd^{2+} eliminates bursts without affecting the
543 underlying burstlet rhythm (**Kam et al., 2013a; Sun et al., 2019**). However, the rhythmogenic mecha-
544 nism based on percolation is speculative and comes from two experimental observations. The first
545 is that the duration and slope (i.e., shape) of the burstlet onset are statistically indistinguishable
546 from the ramping pre-inspiratory activity that immediately precedes inspiratory bursts (**Kallurkar**
547 **et al., 2020**). We note, however, that this shape of pre-inspiratory activity can arise through intrinsic
548 mechanisms at the individual neuron level (**Abdulla et al., 2021**). The second observation evoked
549 in support of the percolation idea is that holographic photostimulation of small subsets (4 – 9) of
550 preBötC neurons can elicit bursts with delays lasting hundreds of milliseconds (**Kam et al., 2013b**).
551 These delays are longer than could be explained with existing preBötC models and have approxi-
552 mately the same duration as the pre-inspiratory activity and burstlet onset hypothesized to under-
553 lie the rhythm. According to the percolation hypothesis of burstlet rhythm generation, these long
554 delays result from the specific topological architecture of the preBötC, recently proposed to be a
555 heavy-tailed synaptic weight distribution in the rhythmogenic preBötC subpopulation (**Slepukhin**
556 **et al., 2020**).

557 Interestingly, the model presented here naturally captures the long delays characterized by
558 **Kam et al. (2013b)**, and stimulation of small subsets of neurons triggers a growth in population
559 activity in the lead up to a burst that could be described as percolation (Fig. 7B). Our model does
560 not require a special synaptic weight distribution to generate the long delays, however. Indeed,
561 our model suggests that the long delays between simulation and burst generation are due in large
562 part to the dynamics of the pattern-forming population, as probabilistically these neurons are the
563 most likely to be stimulated and they appear to play a dominant role in setting the timing of the
564 elicited burst response (Fig. 8H). Moreover, the dynamics of this population is strongly impacted by
565 the CICR mechanism proposed here, which is required for burst generation. Interestingly, to match
566 the 500 ms refractory period following an endogenous burst during which holographic stimulation
567 cannot elicit a burst, our model predicts that the connection probability in the pattern generating
568 preBötC subpopulation must be between 1% and 2%, which is consistent with available experimen-
569 tal data (**Ashhad and Feldman, 2020**).

570 Thus, taken together, previous modeling and our work offer two alternative, seemingly viable
571 hypotheses about the source of the delay between holographic stimulation and burst onset, each
572 related to a proposed mechanism for burstlet and burst generation. Yet additional arguments
573 call into question aspects of the percolation idea. If the burstlet rhythm is driven by a stochastic
574 percolation process, then the period and amplitude of burstlets should be stochastic, irregular,
575 and broadly distributed. Moreover, in the proposed framework of burstlet theory, the pattern
576 of bursts and burstlets for a given burstlet fraction would also be stochastic, since the burstlet-
577 to-burst transition is thought to be an all-or-none process that depends on the generation of a
578 burstlet of sufficient magnitude. Example traces illustrating a mixture of bursts and burstlets typi-
579 cally show a pattern of multiple burstlets followed by a burst that appears to regularly repeat (**Kam**
580 **et al., 2013b; Sun et al., 2019; Kallurkar et al., 2020**) and hypoglossal output timing has also been
581 found to exhibit high regularity (**Kam et al. (2013b)**), however, suggesting that the burstlet-to-burst
582 transition is not dependent on the synchrony and hence magnitudes of individual burstlets but
583 rather on a slow process that gradually evolves over multiple burstlets. The regularity and pat-

584 terns of burstlets and bursts that arise from such a process in our model match well with those
585 observed experimentally.

586 We note that the burstlet-to-burst transition mechanism proposed here, based on CICR from
587 ER stores, depends on rhythmic inputs from the rhythm-generating to the pattern-generation pop-
588 ulation; however, it is independent of the mechanism of rhythm generation. In our simulations,
589 rhythm generation depends on the slowly inactivating persistent sodium current (I_{NaP}). The role
590 of I_{NaP} in preBötC inspiratory rhythm generation is a contentious topic within the field, largely
591 due to the inconsistent effects of I_{NaP} block. We chose to use I_{NaP} in as the rhythmogenic mech-
592 anism in the burstlet population for a number of reasons: (1) consideration of the pharmacolog-
593 ical mechanism of action and nonuniform effects of drug penetration can explain the seemingly
594 contradictory experimental findings relating to I_{NaP} (**Phillips and Rubin, 2019**), (2) I_{NaP} -dependent
595 rhythm generation is a well-established and understood idea (**Butera et al., 1999**), (3) recent com-
596 putational work on which the current model is based suggests that rhythm generation occurs in a
597 small, I_{NaP} -dependent rhythmogenic kernel that is analogous to the burstlet population (**Phillips**
598 *et al., 2019*), and predictions from this model that depend on the specific proposed roles of I_{NaP}
599 and I_{CAN} in rhythm and pattern formation have been experimentally confirmed in a recent study
600 (**Phillips et al., 2021**). It is important to note, however, that the findings about burstlets and bursts
601 presented in this work would have been obtained if the burstlet rhythm was imposed (Fig. 1) or if
602 burstlets were generated by some other means, such as by the percolation mechanism proposed
603 by burstlet theory.

604 **Conclusions**

605 This study has developed the first model-based description of the biophysical mechanism under-
606 lying the generation of bursts and burstlets in the inspiratory preBötC. As suggested by burstlet
607 theory and other previous studies, rhythm and pattern generation in this work are represented
608 by two distinct preBötC subpopulations. A key feature of our model is that generation of network
609 bursts (i.e. motor output) requires amplification of postsynaptic Ca^{2+} transients by CICR in order to
610 activate I_{CAN} and drive bursting in the rest of the network. Moreover, the burstlet fraction depends
611 on rate of Ca^{2+} buildup in intracellular stores, which is impacted by K_{bath} -dependent modulation
612 of preBötC excitability. These ideas complement other recent findings on preBötC rhythm genera-
613 tion (**Phillips et al., 2019; Phillips and Rubin, 2019; Phillips et al., 2021**), together offering a unified
614 explanation for a large body of experimental findings on preBötC inspiratory activity that offer a
615 theoretical foundation on which future developments can build.

616 **Methods and Materials**

617 **Neuron Model**

618 Model preBötC neurons include a single compartment and incorporate Hodgkin-Huxley style con-
619 ductances adapted from previously described models (**Jasinski et al., 2013; Phillips et al., 2019;**
620 **Phillips and Rubin, 2019**) and/or experimental data as detailed below. The membrane potential of
621 each neuron is governed by the following differential equation:

$$C \frac{dV}{dt} = -I_{Na} - I_K - I_{NaP} - I_{Ca} - I_{CAN} - I_{Leak} - I_{Syn} - I_{GIRK} - I_{Holo} + I_{APP}, \quad (1)$$

622 where $C = 36\text{ pF}$ is the membrane capacitance and each I_i represents a current, with i denoting the
623 current's type. The currents include the action potential generating Na^+ and delayed rectifying K^+
624 currents (I_{Na} and I_K), persistent Na^+ current (I_{NaP}), voltage-gated Ca^{2+} current (I_{Ca}), Ca^{2+} -activated
625 non-selective cation (CAN) current (I_{CAN}), K^+ dominated leak current (I_{Leak}), synaptic current (I_{Syn}),
626 μ -opioid receptor activated G protein-coupled inwardly-rectifying K^+ current (I_{GIRK}), and a holo-
627 graphic photostimulation current (I_{Holo}). I_{APP} denotes an applied current injected from an elec-
628 trode. The currents are defined as follows:

$$I_{Na} = g_{Na} \cdot m_{Na}^3 \cdot h_{Na} \cdot (V - E_{Na}) \quad (2)$$

Table 1. Ionic Channel Parameters.

Channel	Parameters				
I_{Na}	$g_{Na} = 150 \text{ nS}$ $m_{1/2} = -43.8 \text{ mV}$ $h_{1/2} = -67.5 \text{ mV}$	$E_{Na} = 26.54 \cdot \ln(Na_{out}/Na_{in})$ $k_m = 6.0 \text{ mV}$ $k_h = -11.8 \text{ mV}$	$Na_{in} = 15 \text{ mM}$ $\tau_{max}^m = 0.25 \text{ ms}$ $\tau_{max}^h = 8.46 \text{ ms}$	$Na_{out} = 120 \text{ mM}$ $\tau_{1/2}^m = -43.8 \text{ mV}$ $\tau_{1/2}^h = -67.5 \text{ mV}$	$k_\tau^m = 14.0 \text{ mV}$ $k_\tau^h = 12.8 \text{ mV}$
I_K	$g_K = 220 \text{ nS}$ $A_\alpha = 0.011$ $A_\beta = 0.17$	$E_K = 26.54 \cdot \ln(K_{bath}/K_{in})$ $B_\alpha = 44.0 \text{ mV}$ $B_\beta = 49.0 \text{ mV}$	$K_{in} = 125$ $k_\alpha = 5.0 \text{ mV}$ $k_\beta = 40.0 \text{ mV}$	$K_{Bath} = VAR$	
I_{NaP}	$g_{NaP} = N(\mu, \sigma)$, See Table 2 $m_{1/2} = -47.1 \text{ mV}$ $h_{1/2} = -60.0 \text{ mV}$	$E_{NaP} = 26.54 \cdot \ln(Na_{out}/Na_{in})$ $k_m = 3.1 \text{ mV}$ $k_h = -9.0 \text{ mV}$	$\tau_{max}^m = 1.0 \text{ ms}$ $\tau_{max}^h = 5000 \text{ ms}$	$\tau_{1/2}^m = -47.1 \text{ mV}$ $\tau_{1/2}^h = -60.0 \text{ mV}$	$k_\tau^m = 6.2 \text{ mV}$ $k_\tau^h = 9.0 \text{ mV}$
I_{Ca}	$g_{Ca} = 0.0065 \text{ pS}$ $m_{1/2} = -27.5 \text{ mV}$ $h_{1/2} = -52.4 \text{ mV}$	$E_{Ca} = 13.27 \cdot \ln(Ca_{out}/Ca_{in})$ $k_m = 5.7 \text{ mV}$ $k_h = -5.2 \text{ mV}$	$\tau_m = 0.5 \text{ ms}$ $\tau_h = 18.0 \text{ ms}$	$Ca_{out} = 4.0 \text{ mM}$	
I_{CAN}	$g_{CAN} = N(\mu, \sigma)$, See Table 2	$E_{CAN} = 0.0 \text{ mV}$		$Ca_{1/2} = 0.00074 \text{ mM}$	$n = 0.97$
I_{Leak}	$g_{Leak} = N(\mu, \sigma)$, See Table 2	$E_{Leak} = -26.54 \cdot \ln[(P_{Na} * Na_{in} + P_K * K_{in}) / (P_{Na} * Na_{out} + P_K * K_{bath})]$			
	$P_{Na} = 1$	$P_K = 42$			
I_{Syn}	$g_{Syn} = VAR$, See Eq. 25	$E_{Syn} = 0.0 \text{ mV}$	$\tau_{Syn} = 5.0 \text{ ms}$		
I_{GIRK}	$g_{GIRK} = 0 - 0.3 \text{ nS}$	$E_{GIRK} = E_K$			
I_{Holo}	$g_{Holo} = 50 \text{ nS}$	$\tau_{Holo} = 100 \text{ ms}$	$E_{Holo} = E_{Syn}$		

$$I_K = g_K \cdot m_K^4 \cdot (V - E_K) \quad (3)$$

$$I_{NaP} = g_{NaP} \cdot m_{NaP} \cdot h_{NaP} \cdot (V - E_{Na}) \quad (4)$$

$$I_{Ca} = g_{Ca} \cdot m_{Ca} \cdot h_{Ca} \cdot (V - E_{Ca}) \quad (5)$$

$$I_{CAN} = g_{CAN} \cdot m_{CAN} \cdot (V - E_{CAN}) \quad (6)$$

$$I_{Leak} = g_{Leak} \cdot (V - E_{Leak}) \quad (7)$$

$$I_{Syn} = g_{Syn} \cdot (V - E_{Syn}) \quad (8)$$

$$I_{GIRK} = g_{GIRK} \cdot (V - E_K) \quad (9)$$

$$I_{Holo} = g_{Holo} \cdot (V - E_{Syn}) \quad (10)$$

where g_i is the maximum conductance, E_i is the reversal potential, and m_i and h_i are gating variables for channel activation and inactivation for each current I_i . The glutamatergic synaptic conductance g_{Syn} is dynamic and is defined below. The values used for the g_i and E_i appear in Table 1.
Activation (m_i) and inactivation (h_i) of voltage-dependent channels are described by the following differential equation:

$$\tau_X(V) \cdot \frac{dX}{dt} = X_\infty(V) - X; \quad X \in \{m, h\} \quad (11)$$

Table 2. Distributed channel conductances.

Type	g_{NaP} (nS)		g_{Leak} (nS)		g_{CAN} (nS)	
	μ	σ	μ	σ	μ	σ
Rhythm	3.33	0.75	$(K_{Bath} - 3.425)/4.05$	$0.05 \cdot \mu_{leak}$	0.0	0.0
Pattern	1.5	0.25	$(K_{Bath} - 3.425)/4.05$	$0.025 \cdot \mu_{leak}$	2.0	1.0

634 where X_∞ represents steady-state activation/inactivation and τ_X is a time constant. For I_{Na} , I_{NaP} ,
 635 and I_{Ca} , the functions X_∞ and τ_X take the forms

$$X_\infty(V) = 1/(1 + \exp(-(V - X_{1/2})/k_X)), \quad (12)$$

$$\tau_X(V) = \tau_{max}^X / \cosh((V - \tau_{1/2}^X)/k_\tau^X). \quad (13)$$

636 The values of the parameters ($X_{1/2}$, k_X , τ_{max}^X , $\tau_{1/2}^X$, and k_τ^X) corresponding to I_{Na} , I_{NaP} and I_{Ca} are
 637 given in Table 1.

638 For the voltage-gated potassium channel, the steady-state activation $m_\infty^K(V)$ and time constant
 639 $\tau_m^K(V)$ are given by the expressions

$$m_\infty^K(V) = \alpha_\infty(V)/(\alpha_\infty(V) + \beta_\infty(V)), \quad (14)$$

$$\tau_m^K(V) = 1/(\alpha_\infty(V) + \beta_\infty(V)) \quad (15)$$

640 where

$$\alpha_\infty(V) = A_\alpha \cdot (V + B_\alpha)/(1 - \exp(-(V + B_\alpha)/k_\alpha)), \quad (16)$$

$$\beta_\infty(V) = A_\beta \cdot \exp(-(V + B_\beta)/k_\beta). \quad (17)$$

641 The values for the constants A_α , A_β , B_α , B_β , k_α , and k_β are also given in Table 1.

642 I_{CAN} activation depends on the Ca^{2+} concentration in the cytoplasm ($[Ca]_{Cyto}$) and is given by:

$$m_{CAN} = 1/(1 + (Ca_{1/2}/[Ca]_{Cyto})^n). \quad (18)$$

643 The parameters $Ca_{1/2}$ and n represent the half-activation Ca^{2+} concentration and the Hill coefficient,
 644 respectively, and are included in Table 1.

645 The dynamics of $[Ca]_{Cyto}$ is determined in part by the balance of Ca^{2+} efflux toward a baseline
 646 concentration via the Ca^{2+} pump and Ca^{2+} influx through voltage-dependent activation of I_{Ca} and
 647 synaptically triggered Ca^{2+} transients, with a percentage (P_{SynCa}) of the synaptic current (I_{Syn}) carried
 648 by Ca^{2+} ions. Additionally, the model includes an intracellular compartment that represents
 649 the endoplasmic reticulum (ER), which impacts $[Ca]_{Cyto}$. The ER removes Ca^{2+} from the cytoplasm
 650 via a sarcoplasmic/endoplasmic reticulum Ca^{2+} -ATPase (SERCA) pump, which transports Ca^{2+} from
 651 the cytoplasm into the ER (J_{SERCA}), and releases Ca^{2+} into the cytoplasm via calcium-dependent
 652 activation of the inositol triphosphate (IP3) receptor (J_{IP3}). Therefore, the dynamics of $[Ca]_{Cyto}$ is
 653 described by the following differential equation:

$$\frac{d[Ca]_{Cyto}}{dt} = \alpha_{Ca} \cdot (I_{Ca} + P_{SynCa} \cdot I_{Syn}) + \alpha_{ER} \cdot (J_{IP3} - J_{SERCA}) - \frac{([Ca]_{Cyto} - Ca_{min})}{\tau_{pump}}, \quad (19)$$

654 where $\alpha_{Ca} = 2.5 \cdot 10^{-5} \text{ mM}/fC$ is a conversion factor relating current to rate of change of $[Ca]_{Cyto}$,
 655 $\tau_{pump} = 500 \text{ ms}$ is the time constant for the Ca^{2+} pump, $Ca_{min} = 5.0 \cdot 10^{-6} \text{ mM}$ is a minimal baseline
 656 calcium concentration, and $\alpha_{ER} = 2.5 \cdot 10^{-5}$ is the ratio of free to bound Ca^{2+} in the ER.

657 The flux of Ca^{2+} from the ER to the cytoplasm through the IP3 receptor is modeled as:

$$J_{IP3} = \left(ER_{leak} + G_{IP3} \cdot \left(\frac{[Ca]_{Cyto}}{[Ca]_{Cyto} + K_a} \cdot \frac{[IP3]_i \cdot l}{[IP3]_i + K_l} \right)^3 \right) \cdot ([Ca]_{ER} - [Ca]_{Cyto}), \quad (20)$$

658 where $ER_{leak} = 0.1/mS$ represents the leak constant from the ER stores, $G_{IP3} = 77,500/mS$ represents the permeability of the IP3 channel, $K_a = 1.0 \cdot 10^{-4} mM$ and $K_l = 1.0 \cdot 10^{-3} mM$ are dissociation constants, and $[IP3]_i = 1.5 \cdot 10^{-3} mM$ is the cytoplasm IP3 concentration. Finally, the Ca^{2+} -dependent IP3 gating variable, l , and the Ca^{2+} concentration in the ER, $[Ca]_{ER}$, are determined by the following equations:

$$\frac{dl}{dt} = A \cdot (K_d - l \cdot ([Ca]_{Cyto} + K_d)); \quad (21)$$

$$[Ca]_{ER} = ([Ca]_{total} - [Ca]_{Cyto})/\sigma_{Ca}, \quad (22)$$

663 where $A = 0.1 mM/mS$ is a conversion factor, $K_d = 0.2 \cdot 10^{-3} mM$ is the dissociation constant for IP3
664 inactivation, $[Ca]_{total}$ is the total intracellular calcium concentration and $\sigma_{Ca} = 0.185$ is the ratio of
665 cytosolic to ER volume. The total intracellular calcium concentration is described as:

$$\frac{d[Ca]_{Total}}{dt} = \alpha_{Ca} \cdot (I_{Ca} + P_{SynCa} \cdot I_{Syn}) - \frac{(Ca_{Cyto} - Ca_{min})}{\tau_{pump}}. \quad (23)$$

666 Finally, removal of Ca^{2+} from the cytoplasm by the SERCA pump is modeled as:

$$J_{SERCA} = G_{SERCA} \cdot \frac{[Ca]_{Cyto}^2}{K_{SERCA}^2 + [Ca]_{Cyto}^2}, \quad (24)$$

667 where $G_{SERCA} = 0.45 mM/mS$ is the maximal flux through the SERCA pump, and $K_{SERCA} = 7.5 \cdot 10^{-5} mM$ is a dissociation constant.

669 When we include multiple neurons in the network, we can index them with subscripts. The total
670 synaptic conductance (g_{Syn})_{*i*} of the *i*th target neuron is described by the following equation:

$$(g_{Syn})_i = g_{Tonic} + \sum_{j \neq i, n} W_{j,i} \cdot D_j \cdot C_{j,i} \cdot H(t - t_{j,n}) \cdot e^{-(t-t_{j,n})/\tau_{syn}}, \quad (25)$$

671 where g_{Tonic} is a fixed or tonic excitatory synaptic conductance (e.g., from respiratory control areas
672 outside of the preBötC) that we assume impinges on all neurons, $W_{j,i}$ represents the weight of
673 the synaptic connection from neuron *j* to neuron *i*, D_j is a scaling factor for short-term synaptic
674 depression in the presynaptic neuron *j* (described in more detail below), $C_{j,i}$ is an element of the
675 connectivity matrix ($C_{j,i} = 1$ if neuron *j* makes a synapse with neuron *i* and $C_{j,i} = 0$ otherwise), $H(.)$
676 is the Heaviside step function, and *t* denotes time. τ_{syn} is an exponential synaptic decay constant,
677 while $t_{j,n}$ is the time at which the *n*th action potential generated by neuron *j* reaches neuron *i*.

678 Synaptic depression in the *j*th neuron (D_j) was simulated using an established mean-field model
679 of short-term synaptic dynamics (Abbott et al., 1997; Dayan and Abbott, 2001; Morrison et al., 2008)
680 as follows:

$$\frac{dD_j}{dt} = \frac{D_0 - D_j}{\tau_D} - \alpha_D \cdot D_j \cdot \delta(t - t_j). \quad (26)$$

681 Where the parameter $D_0 = 1$ sets the maximum value of D_j , $\tau_D = 1000 ms$ sets the rate of recovery
682 from synaptic depression, $\alpha_D = 0.2$ sets the fractional depression of the synapse each time neuron
683 *j* spikes and $\delta(.)$ is the Kronecker delta function which equals one at the time of each spike in
684 neuron *j* and zero otherwise. Parameters were chosen to qualitatively match data from Kottick
685 and Del Negro (2015).

686 When we consider a two-neuron network (Fig. 2), we take $W_{1,2} = W_{2,1} = 0.006$ and $C_{1,2} = C_{2,1} = 1$.
687 For the full preBötC population model comprising rhythm and pattern generating subpopulations,
688 the weights of excitatory conductances were uniformly distributed such that $W_{j,i} = U(0, W_{Max})$
689 where W_{Max} is a constant associated with the source and target neurons' populations; with each

such pair, we also associated a connection probability and used this to randomly set the $C_{j,i}$ values (see Table 3). Effects of opioids on synaptic transmission for source neurons in the rhythmogenic subpopulation (Fig. 6) were simulated by scaling $W_{j,i}$ with the parameter $\gamma_{\mu OR}$ which ranged between 0 and 0.5 and sets the percent synaptic block.

Table 3. Maximal synaptic weights and connection probabilities between and within rhythm and pattern generating preBötC subpopulations (W_{Max} , P).

		Target	
		Rhythm	Pattern
Source	Rhythm	(0.15 nS, 0.13)	(0.000175 nS, 0.3)
	Pattern	(0.25 nS, 0.3)	(0.0063 nS, 0.02)

Network construction

The relative proportions of neurons assigned to the rhythm and pattern generating preBötC subpopulations were chosen based on experimental data. For example, *Kallurkar et al. (2020)* found that $20 \pm 9\%$ of preBötC inspiratory neurons are active during burstlets at $K_{Bath} = 9 \text{ mM}$. Moreover, the rhythm and pattern generating neurons are hypothesized to be represented by the subsets of Dbx1 positive preBötC neurons that are somatostatin negative (SST^-) and positive (SST^+), respectively (*Cui et al., 2016; Ashhad and Feldman, 2020*). Somatostatin positive neurons are estimated to comprise 72.6% of the $Dbx1^+$ preBötC population (*Koizumi et al., 2016*). Therefore, our preBötC network was constructed such that the rhythm and pattern forming subpopulations represent 25% and 75% of the $N = 400$ neuron preBötC population (i.e., $N_R = 100$ and $N_P = 300$). The rhythm and pattern generating neurons are distinguished by their I_{NaP} conductances.

The synaptic connection probabilities within the rhythm ($P_{RR} = 13\%$) and pattern ($P_{PP} = 2\%$) generating neurons were taken from previous experimental findings (*Rekling et al. (2000)* and *Ashhad and Feldman (2020)*, respectively). The connection probabilities between the rhythm and pattern generating populations are not known and in the model were set at ($P_{RP} = P_{PR} = 30\%$) such that the total connection probability in the network is approximately 13% (*Rekling et al., 2000*).

Heterogeneity was introduced by normally distributing the parameters g_{leak} , g_{NaP} and g_{CAN} as well as uniformly distributing the weights ($W_{j,i}$) of excitatory synaptic connections; see Tables 2 and 3. Additionally, g_{leak} was conditionally distributed with g_{NaP} in order to achieve a bivariate normal distribution between these two conductances, as suggested by *Del Negro et al. (2002a); Koizumi and Smith (2008)*. In our simulations, this was achieved by first normally distributing g_{NaP} in each neuron according to the values presented in Table 2. Then used a property of bivariate normal distribution which says that the conditional distribution of g_{leak} given g_{NaP} is itself a normal distribution with mean (μ_{Leak}^*) and standard deviation (σ_{Leak}^*) described as follows:

$$\mu_{Leak}^* = \mu_{Leak} + \rho \cdot (\sigma_{Leak}/\sigma_{NaP}) \cdot (g_{NaP}^i - \mu_{NaP}), \quad (27)$$

$$\sigma_{Leak}^* = \sqrt{(1 - \rho^2) \cdot \sigma_{Leak}^2}. \quad (28)$$

Where μ_{Leak} and μ_{NaP} are the mean and, σ_{Leak} and σ_{NaP} are the standard deviation of the g_{Leak} and g_{NaP} distributions. Finally, ρ represents the correlation coefficient and g_{NaP}^i represents the persistent sodium current conductance for the i^{th} neuron. All parameters are given in Table 2.

Activation dynamics of I_{Holo}

Holographic stimulation was simulated by activating I_{Holo} in small sets of randomly selected neurons across the preBötC population. Activation of this current was simulated by the following equa-

725 tion:

$$\frac{dm_{Holo}}{dt} = -\frac{m_{Holo}}{\tau_{Holo}} + \delta(t - t_{stim}). \quad (29)$$

726 Where m_{Holo} represents the channel activation and ranges between 0 and 1, τ_{Holo} represents the
727 decay time constant, and $\delta(\cdot)$ is the Kronecker delta function which represents the instantaneous
728 jump in m_{Holo} from 0 to 1 at the time of stimulation (t_{stim}). Parameters were chosen such that the
729 response in stimulated neurons matched those seen in **Kam et al. (2013b)**. All parameters are
730 given in Table 1.

731 Data analysis and definitions

732 Data generated from simulations was post-processed in Matlab (Mathworks, Inc.). An action potential
733 was defined to have occurred in a neuron when its membrane potential V_m increased through
734 $-35mV$. Histograms of population activity were calculated as the number of action potentials per
735 20 ms bin per neuron, with units of $APs/(s \cdot neuron)$. Network burst and burstlet amplitudes and fre-
736 quencies were calculated by identifying the peaks and the inverse of the interpeak interval from
737 the population histograms. The thresholds used for burst and burstlet detection were $30\text{ spk/s}/N$
738 and $2.5\text{ spk/s}/N$, respectively. For the simulated holographic stimulation simulations, the start of
739 a network burst was defined as the time at which the integrated preBötC population activity in-
740 creased through the threshold for burst detection, while the end of a network burst was defined
741 as the time at which the integrated preBötC activity returned to exactly zero.

742 Integration methods

743 All simulations were performed locally on an 8-core Linux-based operating system or on compute
744 nodes at the University of Pittsburgh's Center for Research Computing. Simulation software was
745 custom written in C++. Numerical integration was performed using the first-order Euler method
746 with a fixed step-size (Δt) of $0.025ms$. All model codes will be made freely available through the
747 ModelDB sharing site hosted by Yale University upon publication of this work.

748 **Supplementary Material**

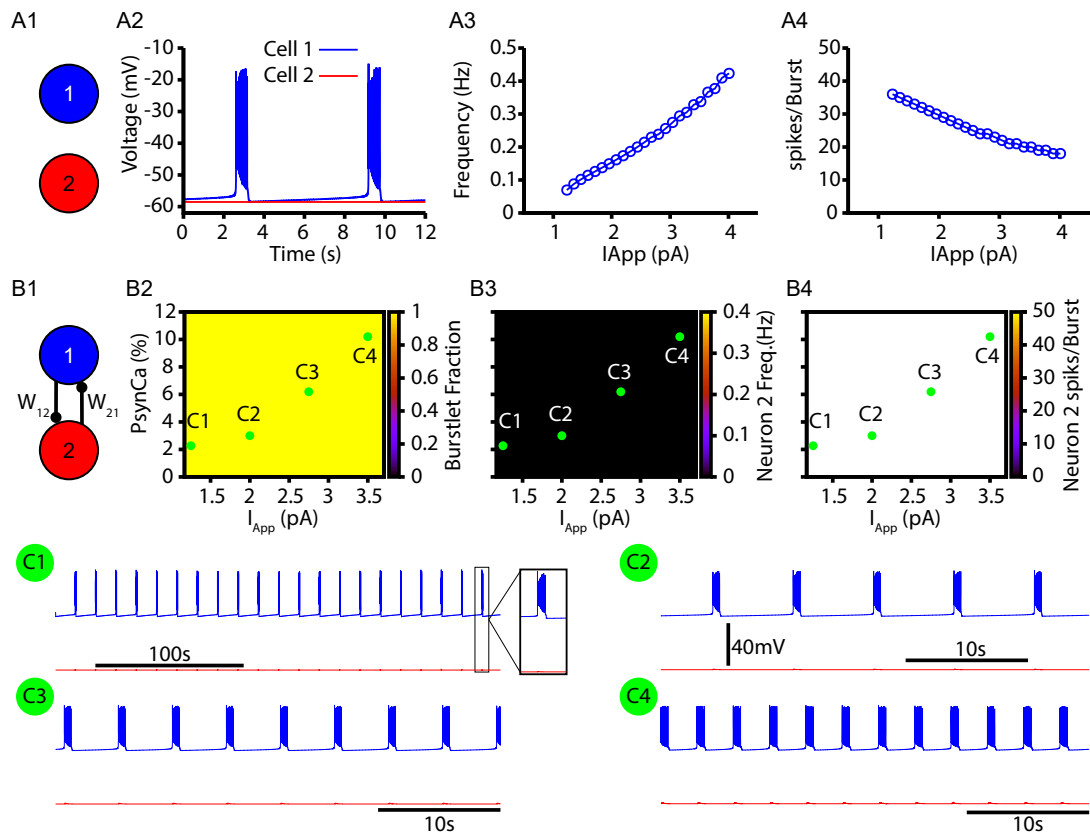


Figure 2-Figure Supplement 1. Without CICR, the two neuron network fails to generate bursts (recruitment of neuron 2). These simulations are identical to those in Fig. 2 except the conductance of the IP₃ receptor is set to zero ($G_{IP_3} = 0/\text{ms}$). (A1) Schematic diagram of the synaptically uncoupled network. The rhythm and pattern generating components of the network are represented by neuron 1 and 2, respectively. (A2) Example trace showing intrinsic bursting in neuron 1 and quiescence in neuron 2. (A3) Burst frequency and (A4) the number of spikes per burst in neuron 1 as a function of an applied current (I_{App}). Neuron 2 remained quiescent within this range of I_{App} . (B1) Schematic diagram of the synaptically coupled network. (B2-B4) 2D plots characterizing the (B2) burstlet fraction, (B3) neuron 2 (burst) frequency, and (B4) neuron 2 spikes per burst (burst amplitude) as a function of I_{App} and P_{SynCa} . (C1-C4) Example traces for neuron 1 and 2 for various I_{App} and P_{SynCa} values indicated in (B2-B4). Notice that neuron 2 is never recruited by the bursting in neuron 1 for any of the conditions tested. The model parameters used in these simulations are: (neuron 1 & 2) $K_{Bath} = 8 \text{ mM}$, $g_{Leak} = 3.35 \text{ nS}$, $W_{12} = W_{21} = 0.006 \text{ nS}$; (Neuron 1) $g_{NaP} = 3.33 \text{ nS}$, $g_{CAN} = 0.0 \text{ nS}$, Neuron 2 $g_{NaP} = 1.5 \text{ nS}$, $g_{CAN} = 1.5 \text{ nS}$.

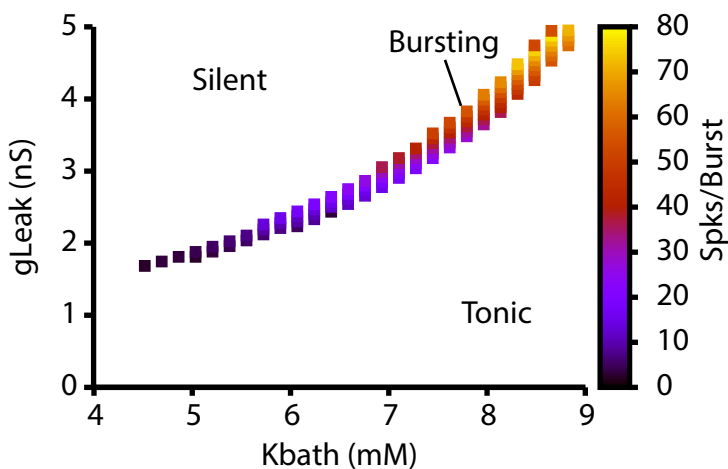


Figure 3-Figure Supplement 1. Dependence of intrinsic cellular dynamics and the number of spikes per burst on K_{bath} and g_{Leak} . For these simulations $g_{NaP} = 5.0 \text{ nS}$.

References

- 749
750 Abbott LF, Varela J, Sen K, Nelson S. Synaptic depression and cortical gain control. *Science*. 1997; 275(5297):221–224.
751
752 Abdulla MU, Phillips RS, Rubin JE. Dynamics of ramping bursts in a respiratory neuron model. *Journal of computational neuroscience*. 2021; [doi: https://doi.org/10.1007/s10827-021-00800-w](https://doi.org/10.1007/s10827-021-00800-w).
753
754 Ashhad S, Feldman JL. Emergent elements of inspiratory rhythmogenesis: network synchronization and synchrony propagation. *Neuron*. 2020; 106(3):482–497.
755
756 Bacak BJ, Kim T, Smith JC, Rubin JE, Rybak IA. Mixed-mode oscillations and population bursting in the pre-Bötzinger complex. *Elife*. 2016; 5:e13403.
757
758 Bachmutsky I, Wei XP, Kish E, Yackle K. Opioids depress breathing through two small brainstem sites. *Elife*. 2020; 9:e52694.
759
760 Baertsch NA, Bush NE, Burgraff NJ, Ramirez JM. Dual mechanisms of opioid-induced respiratory depression in the inspiratory rhythm generating network. *bioRxiv*. 2021; .
761
762 Baertsch NA, Baertsch HC, Ramirez JM. The interdependence of excitation and inhibition for the control of dynamic breathing rhythms. *Nature communications*. 2018; 9(1):1–17.
763
764 Bertram R, Rubin JE. Multi-timescale systems and fast-slow analysis. *Mathematical Biosciences*. 2017; 287:105–121.
765
766 Butera RJ, Rinzel J, Smith JC. Models of respiratory rhythm generation in the pre-Bötzinger complex. I. Bursting pacemaker neurons. *Journal of neurophysiology*. 1999; 82(1):382–397.
767
768 Crowder EA, Saha MS, Pace RW, Zhang H, Prestwich GD, Del Negro CA. Phosphatidylinositol 4, 5-bisphosphate regulates inspiratory burst activity in the neonatal mouse preBötzinger complex. *The Journal of physiology*. 2007; 582(3):1047–1058.
769
770
771 Cui Y, Kam K, Sherman D, Janczewski WA, Zheng Y, Feldman JL. Defining preBötzinger complex rhythm-and pattern-generating neural microcircuits *in vivo*. *Neuron*. 2016; 91(3):602–614.
772
773 Dayan P, Abbott LF. Theoretical neuroscience: computational and mathematical modeling of neural systems. *Computational Neuroscience Series*; 2001.
774
775 Del Negro CA, Hayes JA, Rekling JC. Dendritic calcium activity precedes inspiratory bursts in preBötzinger complex neurons. *Journal of Neuroscience*. 2011; 31(3):1017–1022.
776
777 Del Negro CA, Koshiya N, Butera Jr RJ, Smith JC. Persistent sodium current, membrane properties and bursting behavior of pre-Bötzinger complex inspiratory neurons *in vitro*. *Journal of neurophysiology*. 2002; 88(5):2242–2250.
778
779

- 780 **Del Negro CA**, Morgado-Valle C, Feldman JL. Respiratory rhythm: an emergent network property? *Neuron*.
781 2002; 34(5):821–830.
- 782 **Del Negro CA**, Morgado-Valle C, Hayes JA, Mackay DD, Pace RW, Crowder EA, Feldman JL. Sodium and calcium
783 current-mediated pacemaker neurons and respiratory rhythm generation. *Journal of Neuroscience*. 2005;
784 25(2):446–453.
- 785 **Del Negro CA**, Wilson CG, Butera RJ, Rigatto H, Smith JC. Periodicity, mixed-mode oscillations, and quasiperi-
786 odicity in a rhythm-generating neural network. *Biophysical Journal*. 2002; 82(1):206–214.
- 787 **Elsen FP**, Ramirez JM. Calcium currents of rhythmic neurons recorded in the isolated respiratory network of
788 neonatal mice. *Journal of Neuroscience*. 1998; 18(24):10652–10662.
- 789 **Feldman JL**, Kam K. Facing the challenge of mammalian neural microcircuits: taking a few breaths may help.
790 *The Journal of physiology*. 2015; 593(1):3–23.
- 791 **Jasinski PE**, Molkov YI, Shevtsova NA, Smith JC, Rybak IA. Sodium and calcium mechanisms of rhythmic bursting
792 in excitatory neural networks of the pre-B ötzinger complex: a computational modelling study. *European*
793 *Journal of Neuroscience*. 2013; 37(2):212–230.
- 794 **Johnson SM**, Smith JC, Funk GD, Feldman JL. Pacemaker behavior of respiratory neurons in medullary slices
795 from neonatal rat. *Journal of neurophysiology*. 1994; 72(6):2598–2608.
- 796 **Kaftan EJ**, Ehrlich BE, Watras J. Inositol 1, 4, 5-trisphosphate (InsP3) and calcium interact to increase the dynamic
797 range of InsP3 receptor-dependent calcium signaling. *The Journal of general physiology*. 1997; 110(5):529–
798 538.
- 799 **Kallurkar PS**, Grover C, Picardo MCD, Del Negro CA. Evaluating the burstlet theory of inspiratory rhythm and
800 pattern generation. *Eneuro*. 2020; 7(1).
- 801 **Kallurkar PS**, Picardo MCD, Sugimura YK, Saha MS, Smith GDC, Del Negro CA. Transcriptomes of Electrophysi-
802 logically Recorded Dbx1-derived Inspiratory Neurons of the preBötzinger Complex in Neonatal Mice. *bioRxiv*.
803 2021; .
- 804 **Kam K**, Worrell JW, Janczewski WA, Cui Y, Feldman JL. Distinct inspiratory rhythm and pattern generating mech-
805 anisms in the preBötzinger complex. *Journal of Neuroscience*. 2013; 33(22):9235–9245.
- 806 **Kam K**, Worrell JW, Ventalon C, Emiliani V, Feldman JL. Emergence of population bursts from simultaneous
807 activation of small subsets of preBötzinger complex inspiratory neurons. *Journal of Neuroscience*. 2013;
808 33(8):3332–3338.
- 809 **Koizumi H**, John TT, Chia JX, Tariq MF, Phillips RS, Mosher B, Chen Y, Thompson R, Zhang R, Koshiya N,
810 et al. Transient receptor potential channels TRPM4 and TRPC3 critically contribute to respiratory mo-
811 tor pattern formation but not rhythmogenesis in rodent brainstem circuits. *Eneuro*. 2018; 5(1). doi:
812 <https://doi.org/10.1523/eneuro.0332-17.2018>.
- 813 **Koizumi H**, Mosher B, Tariq MF, Zhang R, Koshiya N, Smith JC. Voltage-dependent rhythrogenic property of
814 respiratory pre-Bötzinger complex glutamatergic, Dbx1-derived, and somatostatin-expressing neuron pop-
815 ulations revealed by graded optogenetic inhibition. *Eneuro*. 2016; 3(3).
- 816 **Koizumi H**, Smith JC. Persistent Na⁺ and K⁺-dominated leak currents contribute to respiratory rhythm gener-
817 ation in the pre-Bötzinger complex in vitro. *Journal of Neuroscience*. 2008; 28(7):1773–1785.
- 818 **Koshiya N**, Smith JC. Neuronal pacemaker for breathing visualized in vitro. *Nature*. 1999; 400(6742):360–363.
- 819 **Kottick A**, Del Negro CA. Synaptic depression influences inspiratory–expiratory phase transition in Dbx1 in-
820 terneurons of the preBötzinger complex in neonatal mice. *Journal of Neuroscience*. 2015; 35(33):11606–
821 11611.
- 822 **Lanner JT**, Georgiou DK, Joshi AD, Hamilton SL. Ryanodine receptors: structure, expression, molecular details,
823 and function in calcium release. *Cold Spring Harbor perspectives in biology*. 2010; 2(11):a003996.
- 824 **Mironov S**. Metabotropic glutamate receptors activate dendritic calcium waves and TRPM channels which
825 drive rhythmic respiratory patterns in mice. *The Journal of physiology*. 2008; 586(9):2277–2291.
- 826 **Morgado-Valle C**, Beltran-Parrazal L, DiFranco M, Vergara JL, Feldman JL. Somatic Ca²⁺ transients do not con-
827 tribute to inspiratory drive in preBötzinger complex neurons. *The Journal of physiology*. 2008; 586(18):4531–
828 4540.

- 829 **Morgado-Valle C**, Fernandez-Ruiz J, Lopez-Meraz L, Beltran-Parrazal L. Substitution of extracellular Ca²⁺ by
830 Sr²⁺ prolongs inspiratory burst in pre-Bötzinger complex inspiratory neurons. *Journal of neurophysiology*.
831 2015; 113(4):1175–1183.
- 832 **Morrison A**, Diesmann M, Gerstner W. Phenomenological models of synaptic plasticity based on spike timing.
833 *Biological cybernetics*. 2008; 98(6):459–478.
- 834 **Okada Y**, Kuwana Si, Kawai A, Mückenhoff K, Scheid P. Significance of extracellular potassium in central res-
835piratory control studied in the isolated brainstem-spinal cord preparation of the neonatal rat. *Respiratory physiol-
836ogy & neurobiology*. 2005; 146(1):21–32.
- 837 **Pace RW**, Mackay DD, Feldman JL, Del Negro CA. Inspiratory bursts in the preBötzinger complex depend on a
838 calcium-activated non-specific cation current linked to glutamate receptors in neonatal mice. *The Journal of physiol-
839ogy*. 2007; 582(1):113–125.
- 840 **Pace RW**, Mackay DD, Feldman JL, Del Negro CA. Role of persistent sodium current in mouse preBötzinger
841 complex neurons and respiratory rhythm generation. *The Journal of physiology*. 2007; 580(2):485–496.
- 842 **Peña F**, Parkis MA, Tryba AK, Ramirez JM. Differential contribution of pacemaker properties to the generation
843 of respiratory rhythms during normoxia and hypoxia. *Neuron*. 2004; 43(1):105–117.
- 844 **Phillips RS**, John TT, Koizumi H, Molkov YI, Smith JC. Biophysical mechanisms in the mammalian respira-
845tory oscillator re-examined with a new data-driven computational model. *eLife*. 2019; 8:e41555. doi:
846 <https://doi.org/10.7554/eLife.41555>.
- 847 **Phillips RS**, Koizumi H, Molkov YI, Rubin JE, Smith JC. Predictions and experimental tests of a new biophysical
848 model of the mammalian respiratory oscillator. *bioRxiv*. 2021; <https://www.biorxiv.org/content/early/2021/11/01/2021.10.29.466442>, doi: [10.1101/2021.10.29.466442](https://doi.org/10.1101/2021.10.29.466442).
- 850 **Phillips RS**, Rubin JE. Effects of persistent sodium current blockade in respiratory circuits depend on the phar-
851macological mechanism of action and network dynamics. *PLoS computational biology*. 2019; 15(8):e1006938.
852 doi: <https://doi.org/10.1371/journal.pcbi.1006938>.
- 853 **Phillips WS**, Del Negro CA, Rekling JC. Dendritic A-Current in Rhythmically Active PreBötzinger Complex Neu-
854rons in Organotypic Cultures from Newborn Mice. *Journal of Neuroscience*. 2018; 38(12):3039–3049.
- 855 **Picardo MCD**, Sugimura YK, Dorst KE, Kallurkar PS, Akins VT, Ma X, Teruyama R, Guinamard R, Kam K, Saha MS,
856 et al. Trpm4 ion channels in pre-Bötzinger complex interneurons are essential for breathing motor pattern
857 but not rhythm. *PLoS biology*. 2019; 17(2):e2006094.
- 858 **Picardo MCD**, Weragalaarachchi KT, Akins VT, Del Negro CA. Physiological and morphological properties of
859 Dbx1-derived respiratory neurons in the pre-Bötzinger complex of neonatal mice. *The Journal of physiology*.
860 2013; 591(10):2687–2703.
- 861 **Rekling JC**, Feldman JL. PreBötzinger complex and pacemaker neurons: hypothesized site and kernel for res-
862piratory rhythm generation. *Annual review of physiology*. 1998; 60(1):385–405.
- 863 **Rekling JC**, Shao XM, Feldman JL. Electrical coupling and excitatory synaptic transmission between rhythmo-
864genic respiratory neurons in the preBötzinger complex. *Journal of Neuroscience*. 2000; 20(23):RC113–RC113.
- 865 **Revill AL**, Katzell A, Del Negro CA, Milsom WK, Funk GD. KNCQ current contributes to inspiratory burst termi-
866nation in the preBötzinger Complex of neonatal rats in vitro. *Frontiers in Physiology*. 2021; 12:305.
- 867 **Rubin JE**, Hayes JA, Mendenhall JL, Del Negro CA. Calcium-activated nonspecific cation current and synaptic de-
868pression promote network-dependent burst oscillations. *Proceedings of the National Academy of Sciences*.
869 2009; 106(8):2939–2944.
- 870 **Salido GM**, Sage SO, Rosado JA. TRPC channels and store-operated Ca²⁺ entry. *Biochimica et Biophysica Acta (BBA)-Molecular Cell Research*. 2009; 1793(2):223–230.
- 871 **Slepukhin VM**, Ashhad S, Feldman JL, Levine AJ. Microcircuit synchronization and heavy tailed synaptic
872 weight distribution in preB\\"otzinger Complex contribute to generation of breathing rhythm. *arXiv preprint arXiv:201212486*. 2020; .
- 873 **Sun X**, Pérez CT, Shao XM, Greenwood M, Heath S, Feldman JL, Kam K, et al. Opioids modulate an emergent
874 rhythmogenic process to depress breathing. *eLife*. 2019; 8:e50613.

- 877 **Tan W**, Janczewski WA, Yang P, Shao XM, Callaway EM, Feldman JL. Silencing preBötzinger complex
878 somatostatin-expressing neurons induces persistent apnea in awake rat. *Nature neuroscience*. 2008;
879 11(5):538–540.
- 880 **Thoby-Brisson M**, Ramirez JM. Identification of two types of inspiratory pacemaker neurons in the isolated
881 respiratory neural network of mice. *Journal of neurophysiology*. 2001; 86(1):104–112.
- 882 **Toporikova N**, Butera RJ. Two types of independent bursting mechanisms in inspiratory neurons: an integra-
883 tive model. *Journal of computational neuroscience*. 2011; 30(3):515–528.
- 884 **Toporikova N**, Chevalier M, Thoby-Brisson M. Sigh and eupnea rhythmogenesis involve distinct interconnected
885 subpopulations: a combined computational and experimental study. *Eneuro*. 2015; 2(2).
- 886 **Tryba AK**, Peña F, Ramirez JM. Stabilization of bursting in respiratory pacemaker neurons. *Journal of Neuro-
887 science*. 2003; 23(8):3538–3546.
- 888 **Wang Y**, Rubin JE. Complex bursting dynamics in an embryonic respiratory neuron model. *Chaos: An Interdis-
889 ciplinary Journal of Nonlinear Science*. 2020; 30(4):043127.